Determining the evolution of the relativistic jet properties in X-ray binary MAXI J1836−194

T. F. Aarhus

May 19, 2023

Abstract

Despite many years of study, there are still many aspects of astrophysical jets that are still not fully understood. These aspects include topics such as how jets are formed and what it is that sets the jet break frequency. Using computational models to model data from sources launching jets can provide us with valuable information in answering these questions. In this thesis I will present the results of modeling the data from the quasi-simultaneous observation of the X-ray binary MAXI J1836-194 during its 2011 outburst using BHJet, and discuss the evolution of the changing parameters and how they are connected to the changes in the accretion disk and the launching of the jet. Results of the modeling showed a connection between certain parameters and the changing photon index, which were used to connect the theoretical basis for the changing break frequency with the changing photon index.

Contents

1 Introduction **1**

2 Observations **4**

3 Modeling the data **5**
3.1 BHJet . . . 5
3.1.1 Particle distributions . . . 5
3.1.2 Radiation sources . . . 6
3.2 Doppler boosting . . . 9
3.2.1 Jet model assumptions . . . 10
3.3 BHJet parameters . . . 12
3.3.1 Frozen parameters . . . 12
3.3.2 Free parameters . . . 15
3.4 ISIS fitting . . . 18

4 Results **19**
4.1 BHJet parameter evolution over the outburst of MAXI J1836-194 . . . 22

5 Discussion **24**
5.1 Photon index-break frequency connection . . . 24
5.2 Other parameters that don't affect the jet break frequency . . . 26
5.2.1 Evolution of $f_{\rm pl}$ . . . 26
5.2.2 Setting s frozen . . . 27

6 Conclusion and further work **28**

A Other Graphs **29**
A.1 Individual SED fits . . . 29
A.2 Number density . . . 31

B Evolution of parameters with s free **34**

References **36**

List of Figures

1 Particle distribution comparison . . . 6
2 BHJet diagram . . . 10
3 Effect of the parameters . . . 16
4 Light curve of MAXI J1836−194 . . . 19
5 SED plots . . . 20
6 Photon index parameters . . . 24
7 SED fit for September 03 . . . 29
8 SED fit for September 12 . . . 29

9 SED fit for September 17 . . . 30
10 SED fit for September 26 . . . 30
11 SED fit for October 12 . . . 31
12 SED fit for October 27 . . . 31
13 Particle distribution for September 03 . . . 32
14 Particle distribution for September 12 . . . 32
15 Particle distribution for September 17 . . . 32
16 Particle distribution for September 26 . . . 33
17 Particle distribution for October 12 . . . 33
18 Particle distribution for October 27 . . . 33

List of Tables

1 Jet parameters . . . 15
2 Free parameter values . . . 21
3 Jet properties . . . 21
4 Evolution of parameters for free s . . . 34
5 Jet properties for free s . . . 34

1 Introduction

An astrophysical jet is a phenomenon found in many different compact objects, such as pulsars, active galactic nuclei (AGN), and X-ray binaries (XRB). A jet is an ejection of ionized matter from a compact object that may occur when plasma from an accretion disk is approaching the compact object and launched perpendicularly to the accretion disk, along the axis of its rotationDespite decades of study and many proposed models, their launching process is still not fully understood. One aspect that is understood though, is that the launching of jets is connected to changes in the accretion disks around the compact objects.

An X-ray binary is a binary star system consisting of a normal star orbiting a compact object, either a neutron star or a black hole. In these systems, material from the star will be transported towards the compact object; either due to the star orbiting close enough to the compact object for their gravitational potentials to overlap, or due to material from stellar winds being captured by the compact object (Lewin and van der Klis 2006). Because angular momentum is conserved, this material will go in orbit around the compact object, eventually forming an accretion disk. Due to factors such as magnetic tension and viscosity acting on fluid elements of different velocities, the material in the disk will heat up and lose angular momentum by radiating away energy. This causes the material to fall towards the CO, and an accretion disk is formed. The outer disk mostly emits radiation in the optical range, while the innermost part of the disk ($\sim 10R_{\rm g}$) emits X-ray radiation, hence the name.

In addition to the emission from the accretion disk, XRBs can emit X-ray radiation from inverse Comptonization (IC), where relativistic electrons in the jet hit low-energy photons coming from e.g. the disk or companion star, boosting the photons to higher energies. X-ray binaries also emit radiation at other wavelengths, most notably in the radio band. This is due to the effect of the magnetic field from the jet affecting the movement of the electrons, causing them to move helically along the field line, emitting synchrotron radiation in the process.

X-ray binaries spend the majority of their lifetime in a low-luminosity quiescent state due to low levels of accretion which gives the source a low luminosity ($\sim 10^{30-32}$erg s^{-1}), but undergo drastic changes in the radio and X-ray emission during outbursts (Homan and Tomaso Belloni 2005). At the beginning of these outbursts, the source is initially in a so-called Low/Hard state (LH), where the X-ray emission is dominated by a power law-like spectrum with a weak blackbody component (Tananbaum et al. 1972, Remillard and McClintock 2006). The former is believed to come from a geometrically thick, optically thin accretion flow or a jet base, while the latter is from a truncated, geometrically thin, optically thick accretion disk (Shakura and Sunyaev 1973). This state is also associated with steady, partially self-absorbed, compact jets (Dhawan, Mirabel, and Rodríguez 2000, Stirling et al. 2001).

During a typical outburst, the source will transition from the the hard state, go through the intermediate states (first the hard-intermediate state (HIMS) and then soft-intermediate (SIMS) state), until finally settling in the High/Soft (HS) state. In this state, the X-ray spectrum exhibits a blackbody-like spectrum due to a geometrically thin, optically thick accretion disk which extends to the innermost stable circular orbit (ISCO). The ISCO is the smallest stable circular orbit which a test particle can stably orbit the compact object. The jet is not observed in this state, meaning it is either 'dark', (i.e. it doesn't emit radiation) or the jet is quenched.

The current understanding of how outbursts work is that some part of the accretion disk reaches sufficiently high enough temperatures to start ionizing hydrogen due to a switch in the viscosity of

the disk (Meyer and Meyer-Hofmeister 1981, Coriat, R. P. Fender, and Dubus 2012), which leads to an increase in the accretion rate. This leads to heating of the inner disk, leading to more seed photons for the inverse Comptonization, as well as greater radio flux density due to an increase in the matter directed into the jets. Eventually the geometrically thin, optically thick Shakura-Sunyaev disk reaches the innermost stable orbit of the compact object, and replaces the corona supporting the launching of the jet. The source is then in the soft state, where the jet has disappeared, and the spectral energy distribution (SED) of the source can be described with just the emission from the accretion disk. The accretion rate will eventually start to diminish, and the inner accretion disk will evaporate into a corona, and the jet is reestablished. There are also cases where the source will fail to reach the soft state, in which case the outburst will have "failed", though it is not yet fully understood why certain outbursts fail.

In the hard state, the radio spectrum typically follows a power-law ($F(\nu) \propto \nu^{\alpha}$), where $\alpha \geq 0$. This spectrum is due to optically thick synchrotron radiation from the electron population having different energies in different parts of the jet due to cooling processes. Summing up these populations forms the flat SED. The spectrum follows this power-law up to a a given frequency, ν_b, known as the break frequency, where we can see emission from the electron population closest to the BH. Above this frequency the spectrum follows an inverse power-law ($\alpha \sim -0.5$).

At the end of the outburst, the source will gradually transition back through the intermediate states and return to the hard state. During these transitions the jet is formed again. The outburst ends with the source eventually fading back to quiescence.

These outbursts occur relatively frequently, over the course of relatively short time spans (months). This makes XRBs of special interest, as they are excellent laboratories for the study of accretion, and thus the formation of jets.

As already mentioned, there are still many aspects of astrophysical jets that are still not fully understood. Modeling a source using a jet model during its outburst and seeing how the parameters and other properties evolve over time can give more information to help us better understand these aspects. The model I will use for this purpose is a new state-of-the-art jet model called BHJet.

BHJet is a scale invariant, steady-state, multi-zone jet model used for modeling the spectral energy distribution of various astrophysical jet sources such as AGNs, blazars, and X-ray binaries (Lucchini, Ceccobello, et al. 2022, S. Markoff, Nowak, and Wilms 2005, Lucchini, T D Russell, et al. 2020). The BHJet model has its origins in the work of Falcke and Biermann 1995, who built upon the work of Blandford and A. Königl 1979 to give a semi-analytical dynamical jet model in which the disk and jet form a coupled system, enforced by setting the jet power to be proportional to $\dot{M}c^2$. The dynamical treatment was extended by S. Markoff, Falcke, and R. Fender 2001 to give a full multi-zone, multiwavelength model called `agnjet`. This model has undergone several major changes due to certain shortcomings, such as only being able to accelerate to mildly relativistic Lorentz factors ($\gamma \approx 2 - 3$) and violating energy conservation by a factor of ≈ 2 (Patrick Crumley et al. 2017). These issues were addressed and led to an improved dynamical model "flavor" called `bljet`, that uses a Bernoulli approach to treat the jet energy budget and magnetic content of the outflow more self-consistently. The most recent update improved the IC calculation, allowing the code to transition from single to multiple scattering regimes when calculating the SSC component, making it able to handle a larger range of optical depths and electron temperatures.

Prior models only looked at the jet as a single zone, where all the jet emission was assumed to originate from a single, spherical blob of plasma at some location in the jet (Tavecchio, Maraschi, and Gabriele Ghisellini 1998, Böttcher et al. 2013). This new model uses a multi-zone approach

instead, using one of the two model flavors `agnjet` or `bljet`. `agnjet` assumes negligible contribution from the magnetic fields, and the jet is assumed being mildly relativistic and pressure-driven, with efficient particle acceleration. `agnjet` also assumes either adiabatic or quasi-isothermal jets, where the adiabatic model assumes that as the jet expands and propagates, the particles in it will cool adiabatically and don't re-accelerate or re-heat again, while the quasi-isothermal model assumes an unspecified acceleration mechanism (e.g. internal shocks) that re-accelerates the particles, approximately maintaining the electron temperature. `bljet` meanwhile, treats the jet as being mildly magnetized, where most of the particle acceleration comes from the conversion of magnetic field energy into kinetic energy, letting the particles reach arbitrarily high Lorentz factors. Regardless of which model is used in the modeling, several parameters are set when fitting the model to a given SED. These parameters describe various properties of the source such as the disk luminosity, electron temperature in the jet nozzle, and the mass of the black hole, thus giving information of what the source is like based on the observed SED.

In this thesis I will use the data taken during the quasi-simultaneous observation campaign of the XRB MAXI J1836-194 during its 2011 outburst. The source was seen to begin its outburst on August 30 2011 with Monitor of All-sky X-ray Image (MAXI)/Gas Slit Camera (GSC; Matsuoka et al. 2009) on the *International Space Station*(Negoro et al. 2011). It was classified as a black hole candidate (Miller-Jones et al. 2011, D. M. Russell, T. Belloni, et al. 2011, Strohmayer and Smith 2011) with spin $a = 0.88 \pm 0.03$ (Reis et al. 2012) and inclination $4° - 15°$ (T. D. Russell, Soria, Motch, et al. 2014). The source was observed to have transitioned from the hard state to the HIMS on September 11 2011, but rather than continuing this transition to the soft state, the source instead "failed" its outburst and returned to the hard state on 2011 September 28, where it then faded towards quiescence. In this thesis, I will use the data from this outburst and model it using the BHJet model to find the best-fitting parameters. These parameters and other properties of the jet will then be discussed with regards to how they evolve over time, and how they are connected to each other, with a focus on the anti-correlation between the break frequency and the photon index as observed by Koljonen et al. 2015.

In section 2 I go over the data of the outburst, and in section 3 I explain how the BHJet model works and how the data was fitted with the model. Section 4 goes over the results that were obtained from fitting, while section 5 will be a discussion and interpretation of the results of the fitting. A summary and conclusion is provided in section 6.

2 Observations

MAXI J1836-194 was first detected on August 30 2011 by MAXI/GSC, after which more observations of the source were taken with the Karl G. Jansky Very Large Array (VLA) on September 03 2011. Said observations triggered a campaign of further observations during the outburst and its subsequent decay until December 03 2011, though we only consider observations that were quasi-simultaneous with the mid-/near-IR, optical and X-ray data.

The datasets used were provided by Thomas Russell and are the same as the ones that were used in his paper (T. D. Russell, Soria, Miller-Jones, et al. 2014). Some additional changes in the data had to be made before fitting. No simultaneous radio data were observed that coincided with the 2011 October 27 mid-/near-IR and X-ray data, but the source was observed on 2011 October 22 and 2011 November 01. The radio spectrum was thus estimated by simply averaging the spectra over the two dates and assuming that the result corresponded to the radio emission for 2011 October 27. The UV/IR/optical data had to be dereddenend, which was done using the `ccm89` function from the `extinction` module (Cardelli, Clayton, and Mathis 1989). Since absorption due to dust in the interstellar medium is not expected to change significantly over time, $E(B-V) = 0.53$mag was used as a global parameter in the dereddening, with said value being taken from T. D. Russell, Soria, Miller-Jones, et al. 2014. In addition, the X-ray data was rather cluttered, making for difficult to read plots. To make the plots more readable, the X-ray data was split into sets of 20, and their respective frequencies and fluxes were averaged over, reducing the number of data points, and making for better looking plots. It should be noted that this was only done for presenting the plots, the complete set of X-ray data was used when the data was fitted. Lastly, some data points in the X-ray range were removed due to having disproportionately high or low flux, and were dismissed as most likely being noise.

3 Modeling the data

3.1 BHJet

The spectra were modeled using BHJet, a new and improved semi-analytical jet model used to model various jet sources, such as X-ray binaries and active galactic nuclei. How the model works in explained in the following:

3.1.1 Particle distributions

The `BHJet` model works by splitting the jet into multiple zones and calculating the particle distribution in momentum space for each zone. This particle distribution is then used to find the contributions to the SED from the various sources of radiation, e.g. from inverse Comptonization or the accretion disk.

The particle distribution is given in terms of dimensionless momentum, $\varrho = \frac{p}{mc}$, where p is the relativistic momentum, m is the particle mass, and c is the speed of light. The Lorentz factor of the particles is then $\gamma = \sqrt{\varrho^2 + 1}$. BHJet supports five different types of particle distributions, though for our source and the parameters we chose, only two of them will be used. These two distributions are `Thermal` and `Mixed`. The two distributions used were first introduced in S. Markoff, Falcke, and R. Fender 2001, and further developed in Connors et al. 2016 and Lucchini, T D Russell, et al. 2020. The first distribution, `Thermal`, is a standard Maxwell-Jüttner distribution, used for standard thermal particles:

$$N_{\text{th}}(\varrho) = N_0 \varrho^2 e^{-\frac{\gamma(\varrho)}{\Theta}}, \tag{1}$$

where $\Theta = kT_e/m_e c^2$ is the lepton temperature in units of $m_e c^2$, and N_0 is the normalization, defined as $N_0 = \frac{n}{\int N(\varrho) d\varrho}$, where n is the particle number density.

`NonThermal` is one of the unused particle distributions, and is a non-thermal distribution which can be modeled as a power-law with an exponential cutoff:

$$N_{\text{nth}}(\varrho) = N_0 \varrho^{-s} e^{-\varrho/\varrho_{\max}}, \quad \varrho \geq \varrho_{\min}, \tag{2}$$

where s is the power-law slope, and $\varrho_{\min}$ and $\varrho_{\max}$ are the minimum and maximum momenta.

The second distribution used, `Mixed`, is a combination of `Thermal` and `NonThermal`, defined as

$$N_{\text{mix}}(\varrho) = \begin{cases} (1 - f_{\text{nth}})\, N_{\text{th}}(\varrho) & \varrho < \varrho_{\min} \\ (1 - f_{\text{nth}})\, N_{\text{th}}(\varrho) + f_{\text{nth}} N_{\text{nth}}(\varrho) & \varrho \geq \varrho_{\min} \end{cases} \tag{3}$$

where $\varrho_{\min}$ is the average momentum of the thermal pool. In this distribution, the power-law component thus contains a fraction f_{nth} of the total particle number density n, with the rest being in the thermal pool. This follows the behavior observed in particle-in-cell simulations, as in e.g. Sironi, Petropoulou, and Giannios 2015 and Crumley et al. 2019. The `Thermal` distribution is used for particles at the start of the jet, while the `Mixed` distribution is used in the dissipation region where non-thermal particles are injected. Fig. 1 shows how the two distributions differ from each other. This figure shows the number density as a function of momentum on the left and of the Lorentz factor on the right. The difference between the two is apparent, with the non-thermal distribution having a power-law tail for the higher momenta There is a small discontinuity at the peak of the `Mixed` distribution, but this is negligible for $f_{\text{nth}} < 0.5$. Had I chosen $f_{\text{nth}} > 0.5$ in the modeling, one of the other distributions not covered here would have been used instead.

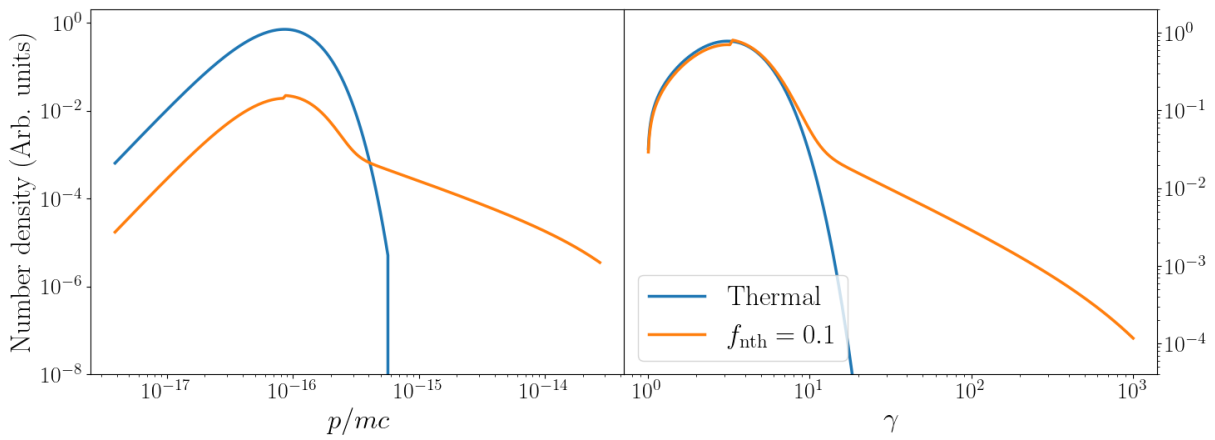

Figure 1: Difference between the two particle distributions used in this thesis. The left panel shows the difference as functions of particle momentum, while the right panel shows it as functions of the Lorentz factor.

All non-thermal particle distributions include methods to calculate the effects of cooling once the particles have reached a steady state. The two methods used in this thesis are radiative and adiabatic cooling, the former causing the particles to lose energy through a given form of radiation, while the latter causes energy loss due to the expansion of the jet. The radiative loss term is defined as (G. Ghisellini, Haardt, and Svensson 1998):

$$\dot{\varrho}_{\rm rad} = \frac{4\sigma_{\rm t} c U_{\rm rad}}{3 m_{\rm e} c^2} \varrho\gamma, \tag{4}$$

where $\sigma_{\rm t}$ is the Thomson cross section, and $U_{\rm rad}$ is the energy density for the appropriate cooling method. The adiabatic loss term is defined as:

$$\dot{\varrho}_{\rm ad} = \frac{\beta_{\rm exp} c}{r} \varrho, \tag{5}$$

where $\beta_{\rm exp}$ is the expansion speed of the emitting region and r its radius. The steady-state particle distribution, assuming constant injection, is then found by solving the equation:

$$N(\varrho) = \frac{\int Q\left(\varrho'\right) d\varrho'}{\dot{\varrho}_{\rm ad} + \dot{\varrho}_{\rm rad}} \tag{6}$$

where Q is the injection term, defined as $N_{\rm mix}(\varrho)/t_{\rm inj}$, where $t_{\rm inj}$ is the injection time, defined as $t_{\rm inj} = r(z)/c$, where $r(z)$ is the radius of the jet.

3.1.2 Radiation sources

The particle distribution is used to calculate the spectral energy distribution for each part of the jet, as the number of particles and their associated momenta affect two of the main sources of radiation. These radiation sources are inverse Comptonization and synchrotron radiation from the jet. BHJet uses the classes `Compton` and `Cyclosyn` to model these. Fig. 2 shows a schematic giving a simple model of the different types of radiation and where they come from.

3.1.2.1 Thermal radiation

BHJet also includes the classes `BBody` and `ShSDisk` to model thermal radiation. `BBody` gives standard black-body radiation, which can come from e.g. the companion star or disk irradiation. The black-body model requires a temperature $T_{\mathbf{bb}}$ and a luminosity $L_{\rm bb}$, with the specific luminosity for a given frequency (ν) being calculated as:

$$L_{\rm bb}(\nu) = \frac{L_{\rm bb}}{\sigma_{\rm sb} T_{\rm bb}^4 c^2} \frac{2h\nu^3}{e^{h\nu/kT_{\rm bb}} - 1}, \tag{7}$$

where h is the Planck constant and $\sigma_{\rm sb}$ is the Stefan-Boltzmann constant.

`ShSDisk` models radiation from the accretion disk, modeling it as a Shakura-Sunyaev disk (Shakura and Sunyaev 1973). This class has as parameters the truncation radius, $r_{\rm in}$, the outer radius, $r_{\rm out}$, the viewing angle, θ, and either a luminosity $L_{\rm d}$ or a temperature $T_{\rm in}$ at the ISCO. Assuming a simplified boundary condition (Kubota et al. 1998), $T_{\rm in}$ and $r_{\rm in}$ are connected:

$$T_{\rm in} = \left(\frac{L_{\rm d}}{2\sigma_{\rm sb} r_{\rm in}^2} \right)^{1/4}. \tag{8}$$

The specific luminosity of the disk is calculated as

$$L_{\rm d}(\nu) = \cos(\theta) \int_{r_{\rm in}}^{r_{\rm out}} 4\pi r^2 \frac{h\nu^3}{c^2 (e^{h\nu/kT(r)} - 1)} dr, \tag{9}$$

with $T(r)$ being the standard temperature scaling for an accretion disk, $T(r) \propto (r/r_{\rm in})^{-3/4}$. The disk scale height is taken to be

$$H/R = \max(0.1, L_{\rm d}/L_{\rm Edd}), \tag{10}$$

where $L_{\rm Edd}$ is the Eddington luminosity of the black hole, defined as $L_{\rm Edd} = 1.25 \cdot 10^{38} \left(\frac{M}{M_\odot} \right)$ erg/s, where M is the mass of the black hole, and $M_\odot$ is the mass of the sun.

3.1.2.2 Cyclo-synchrotron radiation

Depending on if the particles are in the relativistic regime or not, the code use either synchrotron or cyclotron radiation, the emission being based on the model by Blumenthal and Gould 1970. For $\gamma > 2$, the particles are in the relativistic regime and emit synchrotron radiation whose standard emissivity is

$$j'_{\rm s}(\nu', \gamma) = \frac{\sqrt{3} e^3 B \sin\theta}{m_{\rm e} c^2} \frac{\nu'}{\nu'_{\rm s}} \int_{\nu'/n u'_{\rm s}}^{\infty} K_{5/3}(y) dy, \tag{11}$$

where ν' is the emitted frequency in the co-moving frame of the emitting region, γ the Lorentz factor of the emitting electrons, B the magnetic field in the emitting region, θ the electron pitch angle, e the electron charge, and $\nu'_{\rm s} = 3eB\gamma^2/4\pi m_{\rm e} c$ is the scale synchrotron frequency. An isotropic distribution of pitch angles is assumed, and an average over them being used.

For $\gamma \leq 2$, the code uses the cyclotron emissivity (G. Ghisellini, Haardt, and Svensson 1998),

$$j'_{\rm c}(\nu', \gamma) = \frac{4\varrho^2}{3} \frac{\sigma_{\rm T} c U_{\rm b}}{\nu_1} \frac{2}{1 + 3\varrho^2} \exp\left[\frac{2(1 - \nu'/\nu'_1)}{1 + 3\varrho^2} \right], \tag{12}$$

where $U_{\rm b} = B^2/8\pi$ is the magnetic energy density in the emitting region, and $\nu_{\rm l} = eB/2\pi m_{\rm e}c$ is the Larmor frequency. Regardless of whether cyclo- or synchrotron radiation is used, the total emissivity is

$$j'(\nu') = \int_{\gamma_{\rm min}}^{\gamma_{\rm max}} N(\gamma) j'_{\rm c,s}(\nu', \gamma) d\gamma, \tag{13}$$

which is an integral over the particle distribution, averaged over all pitch angles. In addition, the absorption coefficient is

$$\alpha'(\nu') = \int_{\gamma_{\rm min}}^{\gamma_{\rm max}} \frac{N(\gamma)}{\gamma^2} \frac{d}{d\gamma} \left(\gamma^2 j'_{\rm c,s}\left(\nu', \gamma\right)\right) d\gamma, \tag{14}$$

and the co-moving luminosity is

$$L'_{\rm s}(\nu') = \frac{16\pi V \nu'^2}{c^2} \frac{j'(\nu')}{\alpha'(\nu')} \left(1 - e^{-\tau'(\nu')}\right), \tag{15}$$

where V is a re-normalising factor depending on the emission region geometry; $V = R^2$ for a sphere of radius R, and $V = HR$ for a cylinder of radius R and height H.

$$\tau'_{\rm s}(\nu') = \frac{\pi}{2\alpha'(\nu') R \delta f(\theta)} \tag{16}$$

is the cyclo-synchrotron optical depth, with $f(\theta) = \sin(\theta)$ for cylindrical emitting regions, and $f(\theta) = 1$ for spherical regions.

3.1.2.3 Inverse Comptonization

Similar to the synchro/cyclotron case, the code uses the inverse Comptonization equations of Blumenthal and Gould 1970. For each lepton Lorentz factor γ, interacting with a photon field with a number density $N(\epsilon_0)$, the scattered photon spectrum in the co-moving frame of the emitting region is

$$\frac{dN}{dt d\epsilon_1} = \frac{2\pi r_{\rm e}^2 m_{\rm e} c^3 N(\epsilon_0) d\epsilon_0}{\gamma \epsilon_0} F_{\rm IC}\left(q, \Gamma_{\rm e}\right), \tag{17}$$

where ϵ_0 and ϵ_1 are the initial and final photon energies, $r_{\rm e}$ is the classical radius of the electron, γ is the electron's Lorentz factor, and $F_{\rm IC}\left(q, \Gamma_{\rm e}\right)$ is defined as

$$F\left(q, \Gamma_{\rm e}\right) = 2q \ln q + (1 + 2q)(1 - q) + \frac{\left(\Gamma_{\rm e} q\right)^2 (1 - q)}{2\left(1 + \Gamma_{\rm e} q\right)}. \tag{18}$$

This term accounts for scattering in the Thomson or Klein-Nishina regime through the quantity $\Gamma_{\rm e} = 4\epsilon\gamma/m_{\rm e}c^2$, occurring in the former for $\Gamma_{\rm e} \ll 1$ and in the latter for $\Gamma_{\rm e} \gg 1$. The quantities q and E_1 are defined as $q = E_1/\left(\Gamma_{\rm e}\left(1 - E_1\right)\right)$, and $E_1 = \epsilon_1/\gamma m_{\rm e}c^2$. The former accounts for photon energy gain from ϵ_0 to ϵ_1 and the latter is the final photon energy in units of the initial electron energy. Integrating over the particle and seed photon distributions gives the spectrum for an individual scattering order:

$$\frac{dN}{dt d\epsilon_1} = \int\int N(\gamma) \frac{dN}{dt d\epsilon_1} d\gamma d\epsilon_0. \tag{19}$$

Multiplying this with $h\epsilon_1$ and the volume of the emitting region V, gives the specific luminosity. If the Thomson optical depth $\tau = n_e \sigma_t R \geq 1$ then only emission from the outer shell of the region is assumed to escape, down to the skin depth for which $\tau = 1$.

Successive scattering orders are calculated by passing the last output of equation 19 into the same equation. The total spectrum is then the sum over all scattering orders:

$$\frac{dN_{\rm tot}}{dtd\epsilon_1} = \sum_i \int\int N(\gamma) \frac{f(T_e, \tau) dN_i}{dtd\epsilon_1} d\gamma d\epsilon_1, \tag{20}$$

where $f(T_e, \tau)$ is a re-normalization factor introduced to take into account the effects of full radiative transfer, escape probability, and pair production/annihilation.

3.1.2.4 Photon fields

Inverse Comptonization requires seed photons, and the model has three ways of inserting the photon fields that are involved. The first method is using the photons from the synchrotron radiation, the second is using photons from black-body radiation, coming from e.g. the companion star, and the last method is using the radiation emitted from the accretion disk.

The first method estimates the target photon distribution as

$$N(\epsilon_0) = \frac{L'_s(\nu')}{ch^2\nu' R^2}, \tag{21}$$

where L'_s and ν' are respectively the luminosity and frequency of the emitted synchrotron photons in the co-moving frame, and R is the radius of the emitting region.

The second assumes a black-body with energy density $U'_{\rm rad}$ and temperature $T'_{\rm bb}$, calculated in the co-moving frame of the emitting region. The photon field is then

$$N(\epsilon_0) = \frac{2U'_{\rm rad}\nu_0^2}{hc^2\sigma_{\rm sb}T'^4_{\rm bb}\left[\exp\left(\epsilon_0/k_b T'_{\rm bb}\right) - 1\right]}, \tag{22}$$

where $\nu_0 = \epsilon_0/h$ is the initial photon frequency.

The final method assumes an optically thick, geometrically thin disk, where the photon distribution is found by integrating the temperature profile along the disk radius:

$$N(\epsilon_0) = \int_{\alpha_{\rm min}}^{\alpha_{\rm max}} \frac{4\pi\nu^2(\delta)}{hc^3\left(e^{h\nu(\delta)/k_b T(\alpha,\delta)} - 1\right)} d\alpha, \tag{23}$$

with $\alpha_{\rm min} = \arctan\left(R_{\rm in}/z\right)$, $\alpha_{\rm max} = \arctan\left(R_{\rm out}/\left(z - HR_{\rm out}/2\right)\right)$ if $z < HR_{\rm out}/2$ and $\alpha_{\rm max} = \pi/2 \arctan\left(R_{\rm out}/\left(z - HR_{\rm out}/2\right)\right)$ otherwise, to account for the change in viewing angle of all the disk regions. $\nu(\delta)$ and $T(\alpha, \delta)$ are the photon frequencies and disk temperatures for each viewing angle, corrected for Doppler beaming if the emitting region is moving with the disk.

3.2 Doppler boosting

Both the cyclo-synchrotron and IC classes track both co-moving and observer frame luminosities with the standard Doppler transformations:

$$L_{c,s}(\nu) = \delta^\alpha L'_{c,s}(\nu'); \quad \nu = \delta\nu' \tag{24}$$

α depends on the emission geometry, with $\alpha = 3$ for spherical regions and $\alpha = 2$ for cylindrical regions.

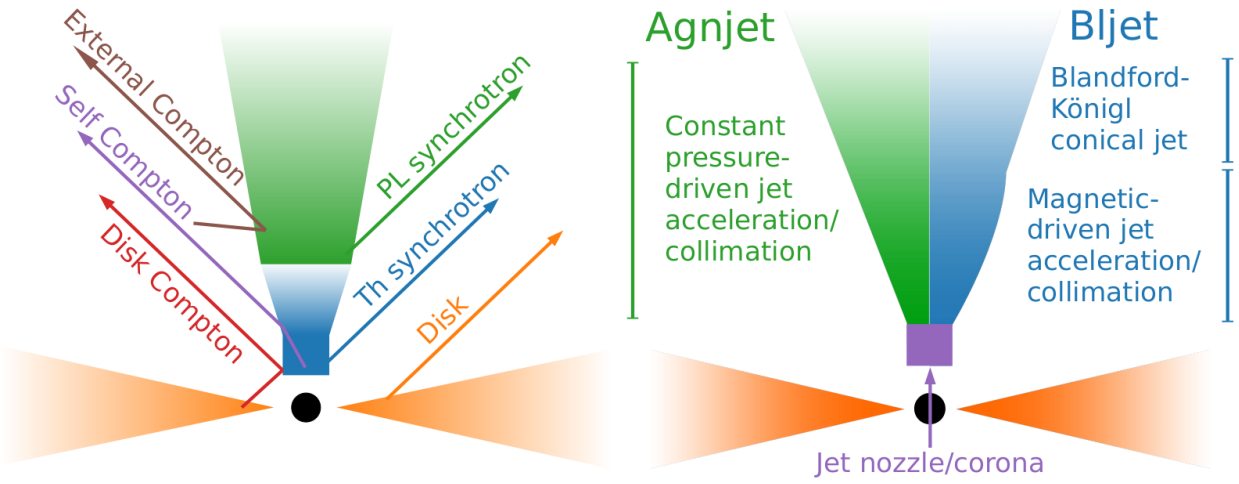

Figure 2: Figure explaining the idea behind the model and the different sources of radiation. Arrows are the types of radiation, and the darker and lighter opacity corresponds to which parts of the jet are more or less bright, respectively. In the left figure, the blue and green components correspond to the thermal and non-thermal parts of the jet, respectively.

3.2.1 Jet model assumptions

In modeling the jet emission with BHJet, various assumptions are made independent of the model flavor or source type. The model assumes that a power N_j is injected into the two jet nozzles given by

$$N_j = 2\pi r_0^2 \beta_0 \gamma_0 c n_{\mathrm{e},0} f_{\mathrm{eq}} \left(\beta_{\mathrm{p}}, \eta, \langle\gamma\rangle\right), \tag{25}$$

where r_0 is the nozzle radius, β_0 is the initial speed, assumed to be $\beta_0 = \sqrt{\Gamma\left(\Gamma-1\right)/\left(\Gamma+1\right)} \approx 0.43$, which is the speed of sound of a relativistic gas with adiabatic index $\Gamma = 4/3$, γ_0 is the initial Lorentz factor of the particles, set to 1.09 by using the value of β_0, and $n_{\mathrm{e},0}$ is the electron number density at the jet nozzle. Lastly, $f_{\mathrm{eq}}(\beta_{\mathrm{p}}, \eta, \langle\gamma\rangle)$ is the equipartition factor, which depends on the model flavor. The equipartition factor depends on the plasma-β parameter, $\beta_{\mathrm{p}} = \frac{U_{\mathrm{e},0}}{U_{\mathrm{b},0}}$, the pair content of the jet, $\eta = \frac{n_{\mathrm{e}}}{n_{\mathrm{p}}}$, and the average Lorentz factor, $\langle\gamma\rangle$. Here $U_{\mathrm{e},0}$ is the energy density of the injected leptons with number density $n_{\mathrm{e},0}$, $U_{\mathrm{b},0}$ is the magnetic field energy density at the base of the jet, and $n_{\mathrm{e},0}$ and $n_{\mathrm{p},0}$ are respectively the initial lepton and proton number densities. Equation 25 can be inverted to find the number density at the base of the jet.

The number density will change as the jet expands and accelerates beyond the nozzle. All flavors assume that the particle number is conserved in the jet, so the number density along the jet can be written as

$$n(z) = n_{\mathrm{e,p},0} \left(\frac{\gamma_0 \beta_0}{\gamma(z)\beta(z)}\right) \left(\frac{r_0}{r(z)}\right)^2, \tag{26}$$

where $n_{\mathrm{e,p},0}$ is the initial number density of either leptons or protons, $\beta(z)$ and $\gamma(z)$ are the jet velocity and Lorentz factor along the z axis, and $r(z)$ is the jet radius at a distance z.

In addition to the above assumptions, specific assumptions are made for each given jet flavor. If the jet terminal Lorentz factor is small and the jet is mildly magnetically dominated ($\sigma_0 \approx$ a few, $\beta_\mathrm{p} \approx 10^{-1} - 10^{-2}$), which is typical for XRBs, then the two model flavors, `agnjet` and `bljet`, are fairly similar, and the choice of model flavor only has a minor impact on the parameters inferred from modeling. Although it's not that important which model flavor is chosen, I chose to use `bljet` in the modeling, as that is the newest and most updated model flavor.

In the following, I go over the assumptions made for `bljet`. As already mentioned, `bljet` assumes that the jet acceleration is powered by conversion of magnetic field energy into bulk kinetic energy, as predicted by ideal magneto-hydrodynamics (MHD) and global general relativistic magneto-hydrodynamic (GRMHD) simulations (e. g. Komissarov et al. 2007 and Tchekhovskoy, McKinney, and Narayan 2009). This acceleration is assumed to be parabolic, in agreement with observations of several AGNs (Boccardi et al. 2015 and Mertens et al. 2016), where the particles are accelerated up to a point γ_acc which is reached at a distance z_acc:

$$\gamma(z) = \gamma_0 + (\gamma_\mathrm{acc} - \gamma_0)\frac{z^{1/2} - z_0^{1/2}}{z_\mathrm{acc}^{1/2} - z_0^{1/2}}. \tag{27}$$

The jet will expand adiabatically as it propagates, and so the jet opening angle and jet radius increase with distance. The opening angle is inversely proportional to the Lorentz factor, as suggested by various very long baseline interferometry (VLBI) observations of *Fermi*/LAT-detected blazars (Pushkarev et al. 2009, Jorstad et al. 2005), and the jet radius depends on this opening angle:

$$\theta(z) = \frac{\rho}{\gamma(z)}, \tag{28}$$

$$r(z) = r_0 + (z - z_0)\tan(\theta(z)) \tag{29}$$

where ρ is inferred from the same VLBI surveys, and is set as $\rho = 0.15$. The magnetic field strength varies with distance as the jet accelerates and is found by imposing energy conservation and solving the Bernoulli equation (Konigl 1980):

$$\gamma(z)\frac{\omega(z)}{n(z)} = \text{const.}, \tag{30}$$

where $\omega(z) = U_\mathrm{p}(z) + U_\mathrm{e}(z) + P_\mathrm{e}(z) + U_\mathrm{b}(z) + P_\mathrm{b}(z)$ is the enthalpy of the jet, and the code assumes that the protons remain cold, therefore having a negligible pressure, and can thus be ignored. The jet magnetization parameter is defined as the ratio of magnetic to particle enthalpy:

$$\sigma(z) = \frac{U_\mathrm{b}(z) + P_\mathrm{b}(z)}{U_\mathrm{p}(z) + U_\mathrm{e}(z) + P_\mathrm{e}(z)}, \tag{31}$$

which reduces to

$$\sigma = \frac{2U_\mathrm{b}(z)}{U_\mathrm{p}(z) + \Gamma U_\mathrm{e}(z)} = \frac{B(z)^2}{4\pi\left(n_\mathrm{p}(z)m_\mathrm{p}c^2 + \Gamma n_\mathrm{e}(z)\langle\gamma_\mathrm{e}\rangle m_\mathrm{e}c^2\right)} \tag{32}$$

if the lepton contribution to the energy budget is negligible. Here $U_\mathrm{b} = \frac{B^2}{8\pi}$ is the magnetic field energy density, $U_\mathrm{p} = n_\mathrm{p}m_\mathrm{p}c^2$ is the energy density of the protons, assumed to be cold, and $U_\mathrm{e} =$

$n_e\langle\gamma\rangle m_e c^2$ is the energy density of the electrons. In this case, the Bernoulli equation, eq. 30, evaluated at z_0 and z_{acc} simplifies to

$$\sigma_0 = (1 + \sigma_{acc}) \frac{\gamma_{acc}}{\gamma_0} - 1, \tag{33}$$

where σ_{acc} is the magnetization at z_{acc}. Given an initial magnetization σ_0, the magnetization along the jet can be written as

$$\sigma(z) = \frac{\gamma_0}{\gamma(z)}(1 + \sigma_0) - 1. \tag{34}$$

Using the definition of the magnetization, 32, this equation can be inverted to find the corresponding magnetic field,

$$B(z) = \left[4\pi\sigma(z)\left(n_p(z)m_p c^2 + \Gamma\langle\gamma_e\rangle n_e(z) m_e c^2\right)\right]^{1/2}. \tag{35}$$

Beyond z_{acc}, the model assumes the standard Blandford and A. Königl 1979 profile, with constant γ_{acc}, constant $\theta_{acc} = \rho/\gamma_{acc}$, a magnetic profile consistent with a toroidal magnetic field, $B(z) \propto z^{-1}$ and continuous particle re-acceleration throughout the jet. The equipartition factor for this jet flavor is

$$f_{eq}\left(\beta_p, \eta, \langle\gamma\rangle\right) = m_p c^2 + \langle\gamma\rangle \eta m_e c^2 \left(1 + \frac{1}{\beta_p}\right), \tag{36}$$

where the ratio of lepton to proton number density becomes

$$\eta = \frac{n_{e,0}}{n_{p,0}} = \frac{m_p}{\langle\gamma\rangle m_e} \frac{\beta_p \sigma_0}{\left(1 + \frac{1}{\beta_p}\right)}. \tag{37}$$

3.3 BHJet parameters

3.3.1 Frozen parameters

BHJet takes in total 27 different parameters as input when generating the spectrum. However, it is recommended that one freezes most of the parameters to an appropriate value before fitting the data. This is done to prevent model degeneracies that could emerge from fitting too many parameters at the same time. The frozen parameters used in this thesis and their values are given in Table 1. In the following, I will go through why they were frozen and why they were set to that particular value:

The black hole mass, inclination of the source, distance to the source, extension of the jet, and radius of the outer disk were all frozen to values based on the suggested values in T. D. Russell, Soria, Miller-Jones, et al. 2014 and table 4 in T. D. Russell, Soria, Motch, et al. 2014. The redshift parameter, z, is set to 0 for our purposes as MAXI J1836-194 is in our galaxy. The maximum extension of the jet is suggested to be frozen to a high value in Lucchini, Ceccobello, et al. 2022 to make the radio spectrum flat, and so was set to $10^9 R_g$. R_{out} is recommended to be frozen and it affects the spectrum negligibly anyway. It was set to its given value based on the tables in T. D. Russell, Soria, Motch, et al. 2014.

f_{nth}, f_{heat}, f_β, and f_{sc} are phenomenological parameters affecting the particle distribution, and are all recommended to be frozen. f_{nth} sets the fraction of non-thermal particles in the particle distribution in the parts of the jet that include non-thermal particles, as described by equation 42. Values typically range between 0.01 and 1, and the parameter is frozen to 0.1. This is consistent

with the efficiency expected for magnetic reconnection and diffusive shock acceleration (Sironi and Spitkovsky 2011, Sironi and Spitkovsky 2014, Sironi, Spitkovsky, and Arons 2013). At $z_{\rm diss}$ the temperature can be increased by a factor $f_{\rm heat}$, with heating, e.g. due to shocks. This parameter lets one indirectly set the minimum Lorentz factor by de-coupling the minimum Lorentz factor of the non-thermal particle distribution from the temperature of the electrons. I opted to set this parameter to unity for simplicity.

s determines the slope of the non-thermal tail of the `Mixed` distribution, as shown in eq. 3. Prior attempts at fitting had s be left free, but due to some apparent degeneracies, as well as slight discrepancies between the fits and prior modelings by Lucchini, T D Russell, et al. 2020, this parameter was instead frozen to a value of 2.2. It was frozen to this value based on examples inLucchini, Ceccobello, et al. 2022 and the values it had during prior fitting attempts where it was left free. The freezing of this parameter and prior fittings with it set free is discussed in more detail in section 5.2.2.

As already mentioned above, the particles in the jet will experience either adiabatic or radiative cooling. f_β sets the value of the adiabatic cooling, as described by equation 5, where f_β takes the value of $\beta_{\rm exp}$. The parameter thus sets the relative importance of the radiative versus adiabatic cooling in the particle distribution given by equation 6, thus also setting the cooling break Lorentz factor $\gamma_{\rm brk}$of the non-thermal distribution. Here, the parameter is set to 0.1, which sets the cooling break Lorentz factor to a relatively low value $\left(10^{1-2}\right)$.

$f_{\rm sc}$ sets the maximum Lorentz factor for the non-thermal particles, either directly, i.e. $f_{\rm sc} = \gamma_{\rm max}$ if $f_{\rm sc} > 10$, or indirectly if $f_{\rm sc} < 0.1$ (values for $f_{\rm sc}$ between 0.1 and 10 are unphysical). In the latter case, $\gamma_{\rm max}$ is found indirectly by balancing the cooling and acceleration timescales of the radiating electrons. The acceleration timescale is defined as

$$t_{\rm acc}(\gamma) = \frac{4\pi_{\rm e} c}{3 f_{\rm sc} e B(z)}, \tag{38}$$

where $B(z)$ is the strength of the magnetic field along the jet. The maximum Lorentz factor is then found via

$$t_{\rm acc}^{-1}(\gamma_{\rm max}) = t_{\rm ad}^{-1}(\gamma_{\rm max}) + t_{\rm rad}^{-1}(\gamma_{\rm max}), \tag{39}$$

where the cooling timescales are defined by eqs. 5 and 4 through $t_{\rm ad,rad} = \varrho / \dot{\varrho}_{\rm ad,rad}$. This balance gives a maximum Lorentz factor of

$$\gamma_{\rm max,pl}(z) = \frac{-3 m_{\rm e} c^2 \beta_{\rm eff}}{8 \sigma_{\rm t} U_{\rm rad}(z) r(z)} + \frac{1}{2}\sqrt{\left(\frac{-3 m_{\rm e} c^2 \beta_{\rm eff}}{4 \sigma_{\rm t} U_{\rm rad}(z) r(z)}\right)^2 + \frac{3 f_{\rm sc} e B(z)}{4 \sigma_{\rm t} U_{\rm rad}(z)}}. \tag{40}$$

Here, the parameter is set to 10^{-6}, giving a relatively low maximum Lorentz factor $\left(\approx 10^3\right)$, as XRBs generally don't have large Lorentz factors (R. P. Fender, T. M. Belloni, and Gallo 2004). The values for $\gamma_{\rm brk}$ and $\gamma_{\rm max}$ are set low in order to suppress the contribution of non-thermal synchrotron radiation to the soft X-ray emission, as there is currently no evidence of jet contribution in the X-rays during outbursts.

The magnetic properties of the system are determined by the parameters $\beta_{\rm p}$ and $\sigma_{\rm acc}$. In `bljet`, β_p is the electron to magnetic field energy density, and indirectly sets the lepton to proton number density and is recommended by Lucchini, Ceccobello, et al. 2022 to always be frozen. σ_{acc} is the leftover magnetization in the jet found at $z_{\rm acc}$, with the magnetization being defined as in eq. 32, (Here, we can ignore the proton pressure, as the protons are assumed to be cold and contribute

negligibly), and is recommended to be frozen to $\sim 0.01 - 1$. We assume a mildly magnetized jet, similar to the example provided in Lucchini, Ceccobello, et al. 2022, and so the values for β_p and σ_{acc} are set to be similar to the values provided there.

`bljet` also has parameters for specific astrophysical scenarios, such as broad line regions (BLR), which are set by the parameters *compsw*, *compar1*, *compar2*, and *compar3*. *compsw* adds either a black body if set to 1, or the (BLR) and dust torus (DT) for an AGN if set to 2 (or adds nothing if set to 0), while the corresponding parameters *compar1*, *compar2*, and *compar3* set the attributes of either the black-body or BLR and DT. *compar1* sets the temperature of the black-body/fraction of disk-photons reprocessed in the BLR, *compar2* sets the luminosity of the BB/fraction of disk photons reprocessed in the Torus, and *compar3* sets energy density of BB or is unused in the case of the BLR/Torus. *compsw* was set to 0 for most dates, with the exception of the dates September 12 and September 17. These dates had a greater flux in the UV/optical/IR range, which required the black-body to be added to give proper fits. *compsw* was thus set to 1. The addition of the black-body is likely due to irradiation from the disk. It should be noted that *compar1* and *compar2* were actually semi-free in the fitting. Originally the parameters were left free for the second and third dates, but this resulted in some unphysical results for the second date. Instead, the parameters were set free for September 17, and frozen to the same values when fitting for September 12.

velsw chooses which model flavor the program uses, using `agnjet` when set to 0 or 1, using either the adiabatic (*velsw*=0) or quasi-isothermal (*velsw*=1) models. Setting *velsw* > 1 uses `bljet`, in which case it will also set the value for $\gamma_{\rm acc}$. Since the `bljet` flavor is used in this thesis, and a mildly relativistic jet is assumed, this parameter was set to 3. I did not include modeling with `agnjet` since the spectrum would deviate little, and although parameters might be different, we are most interested in how they change over time, and they would likely have a similar evolution regardless of the model flavor.

There is one last parameter called *infosw*, but it doesn't affect the fitting, instead setting how much information the program returns, with increasing values giving increasingly more information. Setting it to 1 gives only the plots, while higher values will give particle distributions, and the values of certain jet properties. It was set to 1 when fitting, but was set to 3 to give the number density graphs and other jet properties.

Parameter	Description
Mbh=$8.0 M_\odot$	Mass of the black hole
$\theta = 7.8°$	Inclination of the source
dist = 8.0 kpc	Distance to the source
$z = 0$	Redshift parameter
$z_{\max} = 10^9 R_g$	Maximum extent of the jet
$z_{\rm acc} = z_{\rm diss}$	End of the acceleration region
$f_{\rm nth} = 0.1$	Fraction of non-thermal particles in the jet
$s = 2.2$	Slope of the non-thermal particle distribution
$f_{\rm heat} = 1.0$	Phenomenological parameter imitating shock heating
$f_\beta = 0.1$	Effective adiabatic cooling parameter
$f_{\rm sc} = 10^{-6}$	Sets maximum Lorentz factor of non-thermal particles
$\beta_p = 0.02$	Lepton energy density to magnetic field density
$\sigma_{\rm acc} = 0.1$	Magnetization at $z_{\rm acc}$
$R_{\rm out} = 7 \cdot 10^5 R_g$	Outer radius of the accretion disk
compsw = 1	Switch adding either black-body or Broad Line Region and dust torus
compar1 $= 2.33 \cdot 10^4 K$	Temperature of BB/Fraction of photons processed by BLR
compar2 $= 3.81 \cdot 10^{35}$erg s^{-1}	Luminosity of BB/Fraction of photons processed by Torus
compar3 $= 1.5 \cdot 10^{-5}$erg cm^{-3}	Energy density of BB (unused for compsw=2)
$\gamma_{\rm acc} = 3$	Lorentz factor at $z_{\rm acc}$
infosw=1	Parameter that sets how much information the code prints
N_j ($L_{\rm Edd}$)	Power of the jet
r_0 ($R_{\rm g}$)	Jet nozzle radius
$z_{\rm diss}$ ($R_{\rm g}$)	Start of the dissipation region
$T_{\rm e}$ (keV)	Temperature of leptons in the nozzle
$f_{\rm pl}$	Affects percentage of non-thermal particles and lepton temperature in jet after $z_{\rm diss}$
$L_{\rm disk}$ ($L_{\rm Edd}$)	Luminosity of the disk
$r_{\rm in}$ ($R_{\rm g}$)	Inner radius of the accretion disk

Table 1: The parameters of the jet, along with a description of what they are and what they affect

3.3.2 Free parameters

The remaining parameters were then the jet power, N_j; the jet nozzle radius, r_0; the start of the dissipation region in the jet, $z_{\rm diss}$; the end of the jet acceleration region, $z_{\rm acc}$; the lepton temperature in the jet nozzle, T_e; a phenomenological parameter affecting the particle distribution and temperature after $z_{\rm diss}$, $f_{\rm pl}$; the slope of the non-thermal tail in the particle distribution after $z_{\rm diss}$, s; the disk luminosity, $L_{\rm disk}$; and the inner radius of the accretion disk, $r_{\rm in}$. How these parameters affect the spectrum can be seen in figure 3

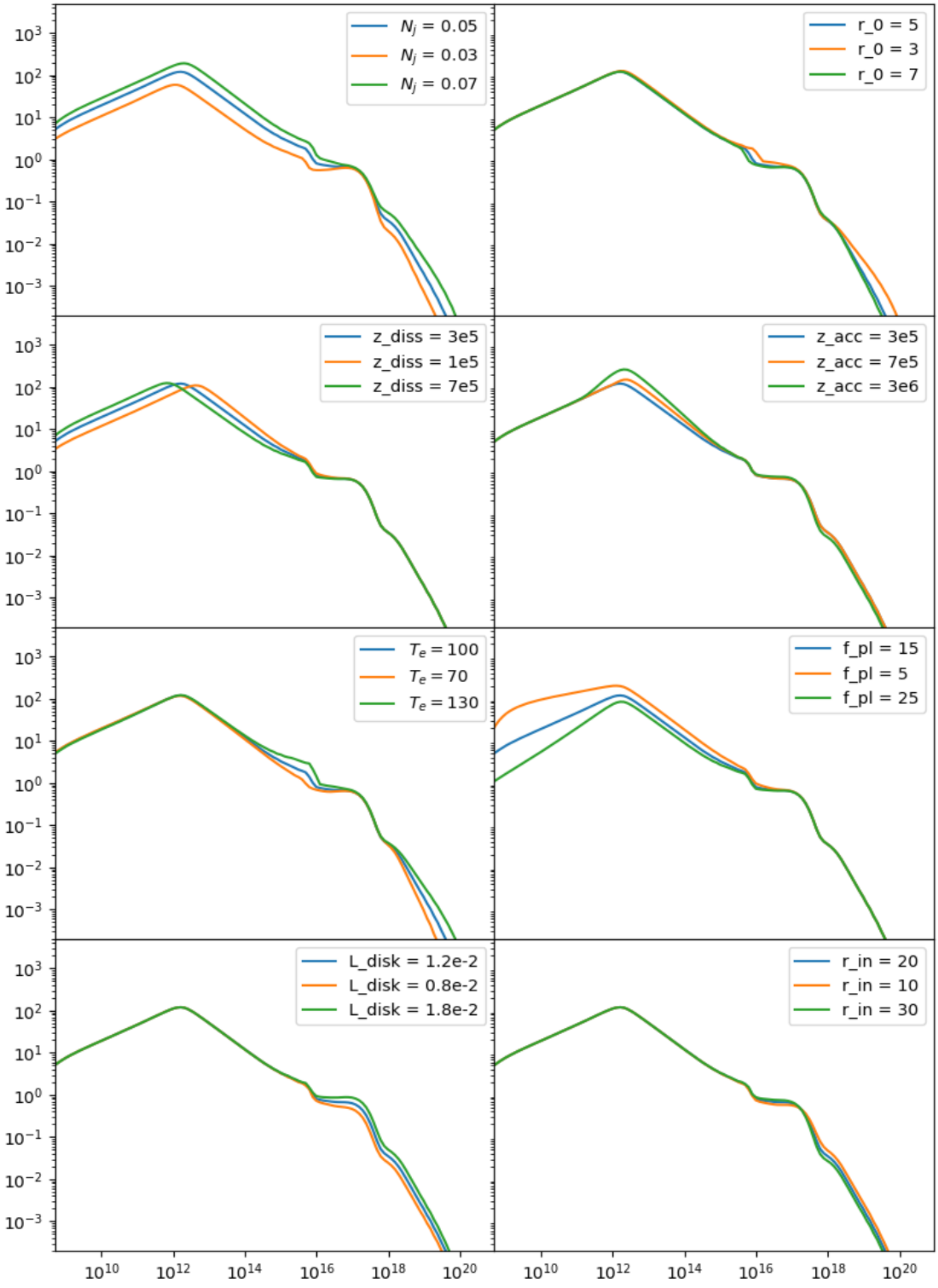

Figure 3: How the different parameters affect the spectrum for a given date.

N_j is the power of the jet in Eddington units, and as the jet power is expected to change during

outburst due to the suppression of the jet as the source transitions to the soft state, this is left free. Fig. 3 shows that this parameter affects the entire spectrum, although less so around 10^{17}Hz, as that section is dominated by radiation from the disk.

r_0 is the radius of the jet base. It also sets the height of the jet nozzle, as the nozzle is assumed to be a cylinder with height z_0 and radius r_0, and with an aspect ratio of $h_\mathrm{r} = z_0/r_0$. h_r is frozen to 2 by default, thus meaning r_0 also sets z_0. This parameter mainly affects the non-thermal synchrotron and IC radiation,

z_diss is the start of an unspecified dissipation region in the jet, where non-thermal particles are injected, due to e.g. shocks or turbulence/shear in the flow. From this point onwards the `Mixed` particle distribution is used. z_diss sets the break frequency indirectly, and is inversely proportional to it. This is due to the fact that an injection of non-thermal particles closer to the compact object results in particles having higher momenta, as they haven't lost as much of their energy through radiative and adiabatic processes as whether they would have from an injection further away. Thus, there will be more high-energy particles that emit synchrotron radiation in higher frequencies, moving the non-thermal synchrotron radiation component to higher frequencies. The reason the break frequency is also moved to higher frequencies is due to the higher optical thickness. Since the optical thickness depends on the radius of the jet,

$$\tau(z) = n(z)r(z)\sigma_\mathrm{t}, \tag{41}$$

and the radius increases as the jet propagates (eq. 29), the optical thickness will be greater closer to the jet nozzle. Since the point of non-thermal particle injection is now at a position in the jet that has higher optical depth, photons that could previously escape the jet are now absorbed, meaning photons of higher energy are now in the optically thick regime. This means that the jet break frequency, the frequency where the spectrum switches from optically thick to optically thin emission, is moved to a higher frequency. Fig. 3 shows how the break frequency moves as z_diss changes. The break frequency for this source was observed to change during its 2011 outburst (Koljonen et al. 2015), typical for XRBs undergoing outbursts. For this reason it should be obvious that this parameter is left free. The inverse relation between z_diss and the break frequency can be seen in fig. 3.

z_acc is, as previously explained, the point at which the particle acceleration ends. Lucchini, Ceccobello, et al. 2022 explains that this parameter is typically set equal to z_diss when using `bljet` to make the location of the non-thermal particle injection highly beamed (Lucchini, Ceccobello, et al. 2022), and that is assumed here as well. Although strictly speaking not a free parameter, it does change over time due to being tied to z_diss. It is therefore included in this section and fig. 3 shows how it affects the spectrum.

T_e is the temperature of the electrons in the nozzle. Fig. 3 shows the areas most affected by changing the temperature. These are the areas where the thermal synchrotron and IC contribute most to the emission. The higher temperature giving greater emission is due to the synchrotron and IC being dependent on the momentum of the electrons, so a higher temperature gives more emission in these regions.

f_pl is a phenomenological parameter and reduces the percentage of non-thermal particles along the jet after z_{diss}, as described by the equation

$$n_\mathrm{nth}(z) = n_\mathrm{nth,0}\left(\frac{\log_{10}(z_\mathrm{diss})}{\log_{10}(z)}\right)^{f_\mathrm{pl}}. \tag{42}$$

Increasing $f_{\rm pl}$ leads to a more inverted radio spectrum, as the radio emission is dominated by non-thermal synchrotron radiation. Reducing the number of non-thermal particles along the jet results in less emission in the lower frequencies, where most of the radiation come from lower-energy particles further down the jet. This effect can be seen in figure 3. Although this helps matching an arbitrarily inverted spectrum, it does deviate slightly from the assumption of an isothermal jet. The parameter also affects the temperature of the jet in the dissipation region, described by a similar formula,

$$T_e(z) = T_e\left(z_{\rm diss}\right)\left(\frac{\log_{10}\left(z_{\rm diss}\right)}{\log_{10}\left(z\right)}\right)^{f_{\rm pl}}. \tag{43}$$

It should be noted that if the jet is mildly relativistic, the inverted radio spectrum can be due to the decrease of the particle density, while if the temperature of the electrons is high and the jet is relativistic, it is mainly driven by the decrease of the electron temperature in the jet instead. As the radio data of MAXI J1836−194 show the radio spectral slope changed over time, it was clear that $f_{\rm pl}$ should be left free. Fig. 3 shows how the slope is affected.

Lastly there's $L_{\rm disk}$ and $r_{\rm in}$, the two parameters affecting the accretion disk, where $L_{\rm disk}$ is the luminosity of the disk in Eddington units, and $r_{\rm in}$ is the inner radius of the disk. During outburst the disk undergoes heating in the inner regions (Lasota 2001), leading to greater luminosity, as per eq. 9. These parameters are thus set free. Fig. 3 shows how they affect the spectrum, mostly in the higher frequencies. This is expected since the higher frequencies are dominated by radiation from the disk and IC, and the latter acquires seed photons from the disk.

3.4 ISIS fitting

To implement model fitting, I used the Interactive Spectral Interpretation System (ISIS) (Houck and Denicola 2000). BHJet includes a wrapper for importing the model into ISIS, making the fitting a simple matter. For the fitting algorithm I opted for `lmdif` which finds the best fit by minimizing the χ^2 error using the Levenberg-Marquardt method (Lourakis 2005). ISIS was also used to probe confidence intervals for the parameters. Starting values for the parameters were taken from the XRB example given in Lucchini, Ceccobello, et al. 2022 or based on prior fitting attempts.

4 Results

I gathered near-simultaneous multiwavelength data from six observing epochs from radio up to X-ray wavelengths. In order to determine the jet properties throughout the outburst I fitted the datasets with the semi-analytical jet model BHJet. In this section, I describe the results of the modeling and the evolution of the parameters following a discussion of the corresponding jet properties. A light curve of the outburst is included in fig. 4, taken from D. M. Russell, T. D. Russell, et al. 2013.

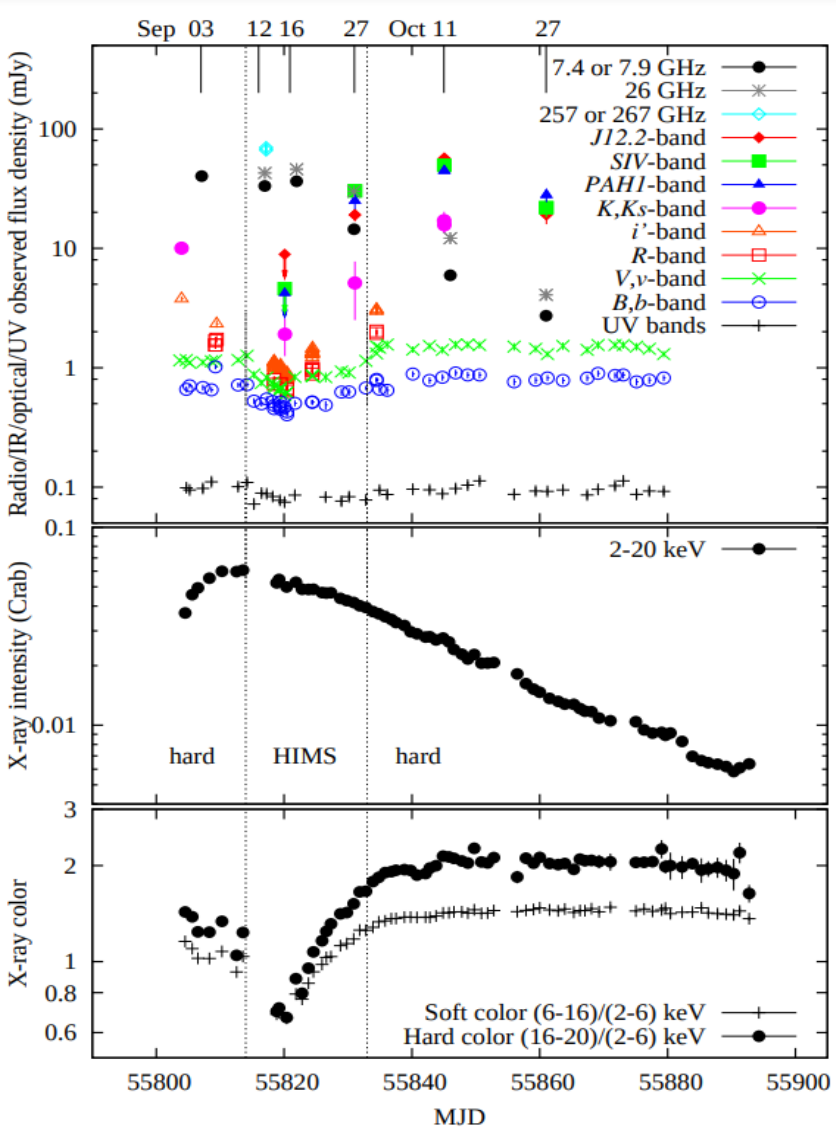

Figure 4: Light curve of the 2011 outburst of MAXI J1836−194. Upper panel: Radio, IR, optical and UV light curves of outburst. Middle panel: X-ray (RXTE) light curve. Lower panel: X-ray color (two intensity ratios are given). The dashed lines represent the state transition dates

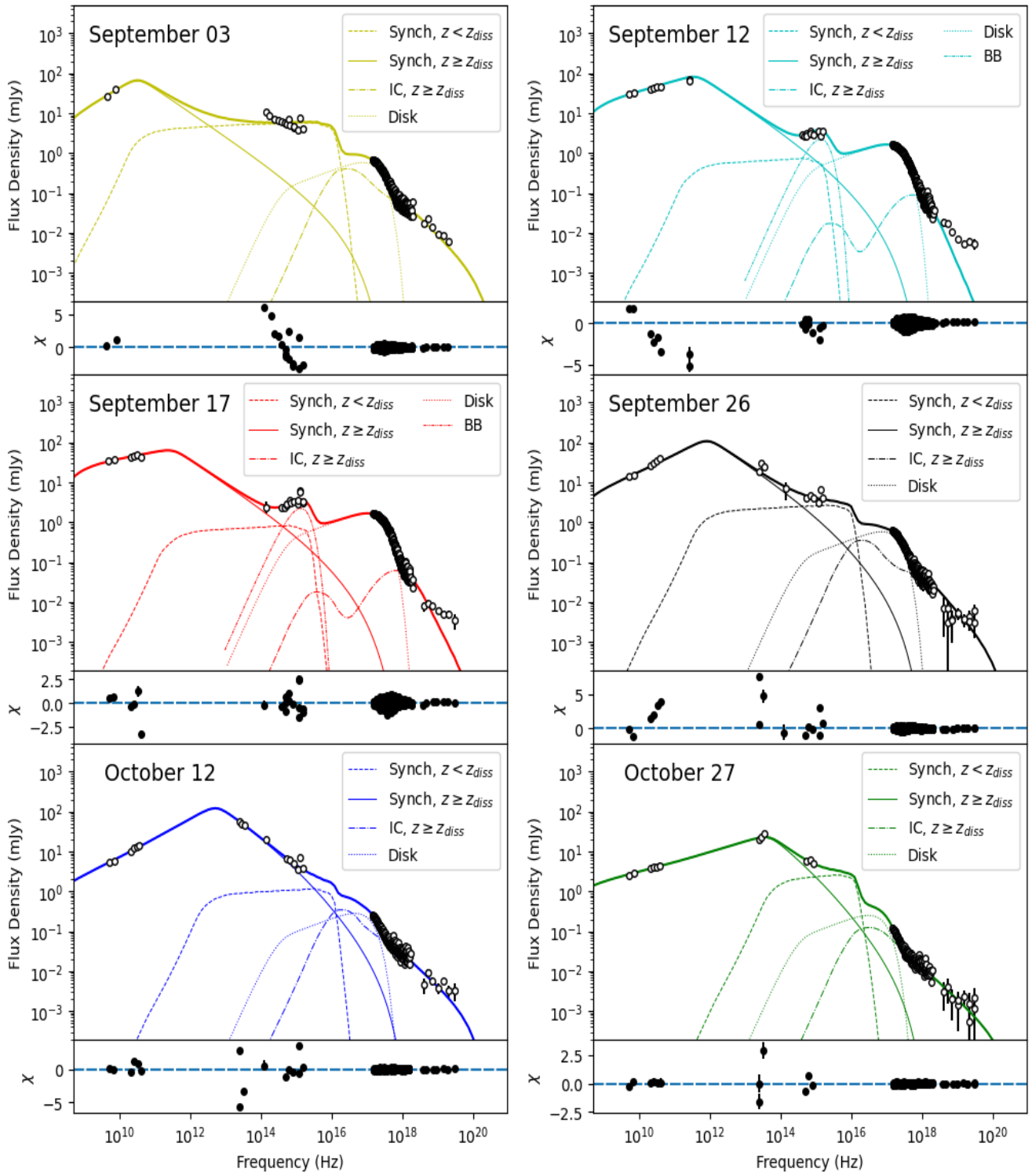

Figure 5: The SEDs and the best-fit BHJet models for the six different observing epoch. The thick line is the total emission, and the thinner lines are the different sources.

The best-fit BHJet models for each of the six observing epochs are shown in figure 5. Enlarged plots of the SED and models for each individual date are included in the appendix for easier reading. In addition to showing the total model and the observed data, the graphs include various model component contributions to the SED: the disk, inverse Comptonization, and synchrotron radiation. The synchrotron radiation is further divided into two separate contributions: a component emitted at the dissipation region where non-thermal particles are injected and a component emitted upstream from the dissipation region where the thermal electrons are accelerated. The model residuals are shown below each panel. The corresponding particle distributions along the jet for each epoch are included in A.2, in figs. 13−18.

The free parameters of the BHJet models and their evolution, as well as the overall model quality are shown in Table 2 for each epoch, and various other properties of the source are shown in Table 3 that are derived from the BHJet parameters.

	03 Sep 2011	12 Sep 2011	17 Sep 2011	26 Sep 2011	12 Oct 2011	27 Oct 2011
Spectral state	Hard	HIMS	HIMS	HIMS	Hard	Hard
$N_j(10^{-2}L_{\rm Edd})$	3.33 ± 0.1	$3.05^{+0.02}_{-0.03}$	$2.12^{+0.02}_{-0.04}$	$4.52^{+0.31}_{-0.15}$	$5.70^{+0.24}_{-0.01}$	$1.37^{+0.06}_{-0.05}$
$r_0(R_g)$	$3.64^{+0.28}_{-0.24}$	13.73 ± 1.0	$9.63^{+0.20}_{-0.49}$	$3.55^{+0.19}_{-0.15}$	$2.62^{+0.23}_{-0.52}$	$2.38^{+0.09}_{-0.15}$
$z_{\rm diss}(R_g)$	$1.43^{+0.07}_{-0.03} \cdot 10^7$	$8.20^{+0.29}_{-0.14} \cdot 10^5$	$8.45^{+6.15}_{-1.35} \cdot 10^5$	$6.53^{+0.24}_{-0.12} \cdot 10^5$	$1.16^{0.32}_{-0.22} \cdot 10^5$	$5.46^{+0.14}_{-0.94} \cdot 10^3$
T_e	$194.3^{6.3}_{-2.1}$	$102.8^{+7.4}_{-5.2}$	$122.3^{+0.8}_{-3.9}$	$136.0^{+5.5}_{-1.2}$	94.5 ± 0.3	$223.4^{+7.9}_{-18.2}$
f_{pl}	$21.5^{+1.7}_{-1.9}$	8.8 ± 0.2	$4.93^{+0.25}_{-0.14}$	$16.9^{+0.2}_{-0.4}$	$19.7^{+0.4}_{-0.3}$	$8.1^{+0.4}_{-0.3}$
$L_{\rm disk}(10^{-2}L_{\rm Edd})$	$1.25^{+0.02}_{-0.01}$	4.29 ± 0.02	4.69 ± 0.01	1.18 ± 0.01	$0.36^{+0.01}_{-0.03}$	$0.21^{+0.02}_{-0.01}$
$r_{\rm in}(R_g)$	$16.53^{+0.27}_{-0.65}$	$20.05^{+0.02}_{-0.01}$	$18.54^{+0.09}_{-0.14}$	$18.01^{+0.7}_{-0.8}$	$24.8^{+2.4}_{-0.8}$	$43.37^{+3.04}_{-9.26}$
χ^2/ d.o.f.	639.4/448	821.7/577	523.5/494	435.7/481	274.6/334	185.7/278
$\chi^2_{\rm red}$	1.43	1.42	1.06	0.91	0.82	0.67

Table 2: The free BHJet parameters and their values for each of the observing epochs. Errors are in the range of ±1 standard deviations, or 68% confidence intervals

	03 Sep 2011	12 Sep 2011	17 Sep 2011	26 Sep 2011	12 Oct 2011	27 Oct 2011
Spectral state	Hard	HIMS	HIMS	HIMS	Hard	Hard
$\alpha_{\rm thick}$	0.51	0.26	0.18	0.42	0.46	0.24
Γ	1.89	3.02	2.69	2.03	1.89	1.84
$\gamma_{\rm avg}$	1.71	1.33	1.41	1.46	1.30	1.85
τ	0.40	0.125	0.12	0.65	1.26	0.23
$\log\nu_b$	10.52	11.52	11.32	11.91	12.71	13.61
$S_{\nu,b}$	66.7	81.1	63.2	107.6	121.4	23.0
$kT_{\rm disk}$(keV)	0.36	0.44	0.47	0.34	0.21	0.14

Table 3: Various derived properties of the jet and how they changed over the observing epochs.

The source was observed in the hard state at the beginning of the observing campaign, exhibiting various properties typical for an X-ray binary in this stateThe jet break frequency was found to be relatively low $\left(\nu_{\rm b} \sim 2 \cdot 10^{11}{\rm Hz}\right)$, and the radio spectrum was inverted ($\alpha_{\rm thick} \sim 0.7$). The source also presented a relatively cool accretion disk, with a moderate luminosity $\left(\sim 1.4 \cdot 10^{-2} L_{\rm Edd}\right)$.

On 2011 September 12, the outburst reached its peak and the X-ray spectrum started to soften.

The source was observed in the HIMS from September 12 to 26 September. During the HIMS an increase in the break frequency was seen, reaching a frequency of $\nu_b \sim 8 \cdot 10^{11}$Hz that remained stable. Also, the radio spectrum flattened ($\alpha_{\text{thick}} \sim 0.2$) until September 26 when it steepened to $\alpha_{\text{thick}} \sim 0.49$. The outburst exhibited a noticeable increase in the disk luminosity, ranging between $\sim 1.4 \cdot 10^{-2} L_{\text{Edd}}$ to $\sim 4 \cdot 10^{-2} L_{\text{Edd}}$.

However, the outburst did not reach a full soft state (i.e. it was a 'failed' outburst) and started its transition back to the hard state some time after September 26. Together with the hardening X-ray spectrum the accretion disk luminosity decreased, and returned to the values it had at the beginning of the spectral campaign around September 26, but continued to decrease further until it was reduced by almost an order of magnitude with respect to the initial luminosity on September 03. Although changing little after the initial outburst, the break frequency underwent a significant change during the spectral hardening, ultimately changing by more than two orders of magnitude compared to the initial state of the source. Lastly, the radio spectrum flattened again on October 27, several days after having returned to the hard state.

4.1 BHJet parameter evolution over the outburst of MAXI J1836-194

Overall, the BHJet parameters evolved according to the expected behavior for an outburst. The disk luminosity increased, the break frequency changed with the source hardness, and the jet was quenched and reformed again during its transition back to the hard state. In this section I will go over the evolving parameters that were found in the fitting process.

The jet power decreased during the HIMS, but started to increase again since the outburst didn't progress to the soft state and transitioned back to the hard state. The diminishing jet power is likely due to the jet starting to quench during the transition. The jet is formed during the transition from soft to hard state, and since the jet power increased during the transition back the increase likely to do with the reformation of the jet. The jet power decreasing again in the final date is likely due to the source fading back to quiescence.

r_0 showed a significant increase once the source had transitioned to the intermediate state, after which it gradually decreased back to the initial value.

f_{pl} and z_{diss} control the slope of the radio spectrum and the jet break frequency respectively. The radio slope was flat during the HIMS, before returning to an inverted slope during the transition back. As the slope is set by f_{pl}, which affects the reduction of non-thermal particles, this implies that the reduction was much less significant during outburst, before returning to pre-HIMS levels as the source returned to the hard state. The flattening of the slope in the final date suggests that the cooling diminished, but this will be discussed further in section 5.2.1. The decrease of z_{diss} after September 17 corresponds to the increase of the break frequency. The decrease from September 03 to September 17, despite the source moving towards the soft state and the photon index increasing, will be discussed further in section **??**.

T_{e} showed a decrease once in the HIMS, but gradually returned to a temperature close to what it was at the beginning of the spectral campaign during its transition back to the hard state.

The evolution of L_{disk} and r_{in} shows how changes in the accretion disk drive the state changes. L_{disk} increases significantly at the beginning of the outburst when it is in the HIMS, but decreases as the source transitions back to the hard state, reducing to a level below what was observed at the start of the campaign. r_{in} didn't change much during outburst, but showed a noticeable increase in the final date.

Table 3 shows the evolution of jet properties inferred from the BHJet parameters, several of which changing how one would expect for an outburst.

The photon index showed behavior similar to the modeling done in Koljonen et al. 2015, showing an increase in the HIMS, but returning to levels similar to those at the start of the campaign when the outburst failed and the source subsequently returned to the hard state.

The jet nozzle opacity, τ, decreased before increasing again during the hard state transition, and eventually decreased again in the final epoch. This property is set by eq. 41, so it is proportional to the number density, and one can see how the initial number density changes by how this property changes.

The other properties correspond more directly to the fitting parameters already discussed, where $\alpha_{\rm thick}$ is set by $f_{\rm pl}$, ν_b by $z_{\rm diss}$, $\gamma_{\rm avg}$ by $T_{\rm e}$, and $kT_{\rm disk}$ by $L_{\rm disk}$.

5 Discussion

In the above, I have described the modeling of six SEDs of the source MAXI J1836-194 during its outburst in 2011 and shown how the various jet parameters have evolved over time. In the following section I will discuss the evolution of the parameters in more detail, focusing on the variable jet break frequency and how it's connected to the other parameters.

5.1 Photon index-break frequency connection

Koljonen et al. 2015 have already reported on an anti-correlation between the position of the break frequency and the value of the photon index in various X-ray binaries, with MAXI J1836-194 being one of them. As shown above, a similar correlation has been replicated for this model, as after the source was in the HIMS state and started to return to the hard state, the photon index decreased and the jet break frequency increased. In the following, this correlation and potential causes for it will be discussed in more detail.

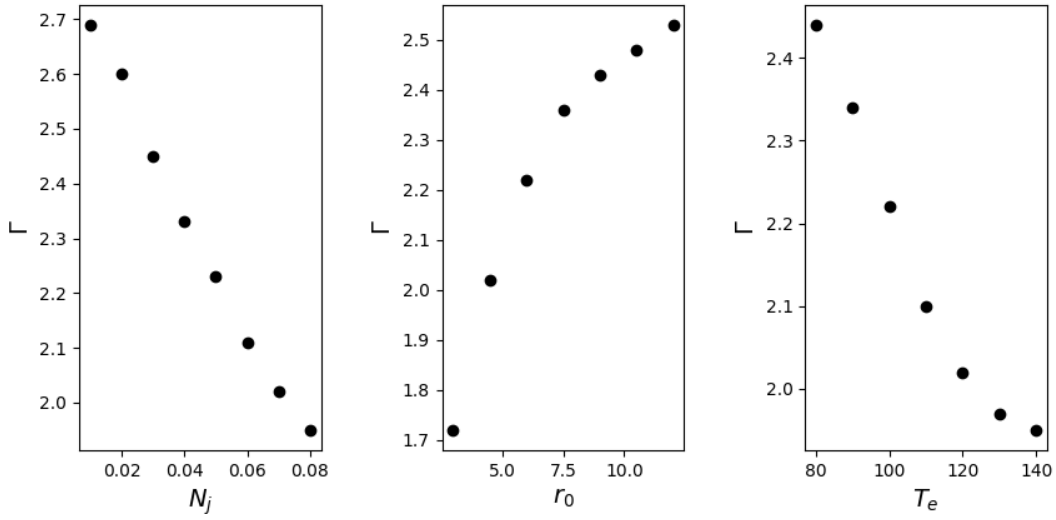

Figure 6: The parameters affecting the photon index, showing how it scales when the parameters are changed. Each panel shows how the photon index changes if all other parameters are kept constant and the one labeled is changed. (Note that this figure is merely meant to illustrate that the parameters affect the photon index and if they are directly or inversely correlated. It shouldn't be taken as a criteria for "how much" the photon index is affected by these parameters, as this can vary depending on the date and other parameters.)

The photon index is related to the spectral index of the X-ray emission (related as $\Gamma = 1 - \alpha$), which in our model is dominated by inverse Comptonization close to the nozzle. The parameters affecting the IC the most are N_j, r_0, and T_e. Fig. 6 shows these parameters and how they affect the photon index. The electron temperature having an inverse correlation with the photon index is likely due to lower temperatures giving lower average momenta for the electrons that partake in the IC process. Lower average momenta means less momentum is transferred in the IC process,

meaning there is a reduction in the higher X-ray emission. In addition, the seed photons from the synchrotron emission will have lower energies because of the lower momenta of the electrons, leading to fewer higher-energy photons.

N_j and r_0 are respectively anti-correlated and correlated with the photon index, and both of these parameters are related to setting the number density in the jet nozzle. As N_j is correlated and r_0 is anti-correlated with the number density, this means the number density is anti-correlated with the photon index. This relation is likely due to a lower number density giving both fewer electrons to transfer their momenta to photons, and fewer seed photons from the synchrotron emission.

The jet break frequency is anti-correlated with $z_{\rm diss}$, and to better understand what sets the location of $z_{\rm diss}$, one needs to look at the theoretical basis for the injection of non-thermal particles. Peter Polko, David L. Meier, and Sera Markoff 2014, building on prior works by P. Polko, D. L. Meier, and S. Markoff 2012, P. Polko, D. L. Meier, and S. Markoff 2010, and Vlahakis and Arieh Königl 2003, developed the theoretical explanation for the observed power-law distribution of particles. They suggested that the non-thermal particles are injected at a shock in the jet. This shock emerges because the jet starts to narrow and overcollimate at a certain point due to e.g. the pressure of the surrounding medium or the magnetic tension of the field lines. This overcollimation leads to shock formation, and the acceleration of particles into a power-law distribution. Since non-thermal emission and the jet break frequency are always observed, this shock has to be a stable feature of the jet. Therefore, the shock has to originate beyond the modified fast point (MFP) of the jet, as the flow beyond this point is causally disconnected from the flow downstream, and cannot disrupt the flow causing it. Combined with the fact that the flow can start to overcollimate around the MFP, means that one can use the location of the MFP as a proxy for the location of the start of the dissipation region. Therefore, I have assumed that the location of $z_{\rm diss}$ is correlated with the location of the MFP. Peter Polko, David L. Meier, and Sera Markoff 2014 show how the location of the MFP is (weakly) correlated with the Alfvén radius, which is the radius of the jet at the Alfvén point, the point where the velocity of the jet equals the Alfvén velocity (a more detailed description is given in the next paragraph). The MFP is also anti-correlated with the angle between the jet axis and the Alfvén point, and the poloidal slope of the field line at the Alfvén point with respect to the accretion disk. In other words, the MFP is closer to the jet nozzle if the Alfvén point lies closer to it too and if the field lines are more cylindrical there.

Establishing the connection between the break frequency (or $z_{\rm diss}$/MFP) and the photon index involves seeing how the parameters affecting the latter can influence what sets $z_{\rm diss}$. The evolution of the parameters after the source has reached the HIMS suggest a trend of decreasing photon index, as shown in Table 3. One can thus establish a connection by showing that the parameters evolving in the way they do leads to a lower MFP. In the above, I explained how $z_{\rm diss}$ is set by the MFP and in the following I will discuss how the BHJet parameters that most affect the photon index also affect the location of the MFP.

The electron temperature can affect the location of the MFP as it's correlated with the Alfvén point. The Alfvén point is the point where the poloidal velocity, V_θ equals the Alfvén velocity, and it is given by

$$(\gamma V_\theta)^2 = \frac{B_\theta^2\left(1-x^2\right)}{4\pi\rho_0\xi}, \tag{44}$$

where ρ_0 is the baryon rest mass, ξ is the relativistic enthalpy, and x is the cylindrical radius in units of the light cylinder radius. The equation taken from eq. 1 from P. Polko, D. L. Meier, and S. Markoff 2010. The temperature sets the average momenta of the particles, and so is directly

correlated with the bulk velocity of the flow. If the flow has a higher bulk velocity, then as the flow is accelerated it will reach the Alfvén velocity sooner, setting the Alfvén point and thus the MFP closer to the jet nozzle. This manifests then as a higher frequency for the jet break, since $z_{\rm diss}$ will also be moved closer. In addition, the Alfvén velocity is inversely related to the enthalpy, which is also related to the temperature. A higher temperature will thus also increase the enthalpy, which lowers the Alfvén velocity, setting the break frequency higher, as already explained.

N_j and r_0 both affect the particle density, as shown by inverting eq. 25:

$$n_{\rm e,0} = \frac{N_j}{2\pi r_0^2 \beta_0 \gamma_0 c f_{\rm eq}\left(\beta_{\rm p}, \eta, \langle\gamma\rangle\right)}. \tag{45}$$

The transition back to the hard state comes with a reformation of the compact jet and an increase in the jet power. The jet nozzle radius also reduces during these dates. These changes contribute to give a higher particle density during these dates. The Alfvén velocity is inversely proportional to the relativistic enthalpy, which is itself proportional the number density. N_j and r_0 therefore contribute in setting a lower Alfvén velocity, which can indirectly set a higher jet break frequency, as already discussed in the previous paragraph. Although only weakly correlated with the MFP/break frequency, r_0 also contributes to setting the Alfvén radius, as r_0 affects what the radius of the jet is at a certain point. A lower Alfvén radius leads to a lower MFP, so if the jet gets narrower over time, the Alfvén radius should also reduce, setting a lower MFP. This is another way the break frequency can be indirectly affected by the changing parameters.

The BHJet model does not take the shape of the magnetic field into account in the modeling, instead simply assuming that it takes the shape of a toroidal field. The fact that the MFP gets closer if the magnetic field lines get more cylindrical is certainly possible, but is not relevant in this case, as our model does not take this into account.

5.2 Other parameters that don't affect the jet break frequency

5.2.1 Evolution of $f_{\rm pl}$

The use of $f_{\rm pl}$ in BHJet to lower the percentage of non-thermal particles/the temperature along the flow after $z_{\rm diss}$ is entirely phenomenological and does not specify any mechanism that is behind the decrease. Essentially, it mimics the effect of additional adiabatic cooling and/or reduced particle acceleration after $z_{\rm diss}$. This parameter decreased during the HIMS, but increased again as it transitioned back to the hard state, suggesting that the cooling/particle reduction was less efficient during the HIMS. It is also of interest that $f_{\rm pl}$ decreased on October 27, contrary to its increasing trend.

The jet power appears to increase/decrease on the same dates as $f_{\rm pl}$. The jet power sets the number density, so if these parameters are connected, one possible interpretation would be to say that the cooling/reduction of the non-thermal particles is connected with the jet power, with a higher jet power giving a greater cooling/reduction.

It should be noted that the interpretation of $f_{\rm pl}$ is somewhat limited due to the parameter being phenomenological, thus making it a bit difficult to interpret it physically. Future models that are able to give a more physical description of the reduced non-thermal particles/temperature would help with this.

5.2.2 Setting s frozen

In modeling the SEDs, the parameter s was initially set free, similar to (Lucchini, T D Russell, et al. 2020). Although this leads to better fits for certain dates, it also leads to some apparent degeneracies between certain parameters. This effectively means that several different parameter combinations give a similar fit quality. There was also the fact that the evolution of the parameters seemed to deviate slightly compared to earlier fitting attempts (Lucchini, T D Russell, et al. 2020). For this reason s was frozen to $s = 2.2$, but I felt it necessary to discuss the earlier fitting where it was set free and discuss its evolution and how the other parameters evolved.

The original parameters where s is kept free are included in section B, Table 4. The jet properties are included in the same section in Table 5 as well. There is a similarity in the evolution of the parameters, although how some of the parameters change is either much more or much less significant. For instance, r_0 shows a much greater increase when transitioning to the HIMS and reaches a lower value in the first epoch, while T_e showed less significant change.

The evolution of s showed an initial increase in the HIMS, but decreased again during its transition back, showing a final increase in the final observing epoch. s sets the slope of the non-thermal particle tail, so the increase of this parameter corresponds to a steeper tail, meaning fewer non-thermal particles in the higher energies. The changing s could correspond to a change in the shock that injects the non-thermal particles, where the dates where s is higher have weaker shocks. Seeing that this parameter changes similar to both N_j and f_pl, it is possible that these parameters can be connected. N_j could affect f_pl as already discussed, while the lower N_j could be connected with what sets the strength of the shocks.

Similar to f_pl, this parameter is more difficult to interpret physically compared to some of the other parameters, so interpretation is again unfortunately more limited.

6 Conclusion and further work

I have modeled six multiwavelength SEDs of the X-ray binary MAXI J1836-194 during its 2011 outburst using a state-of-the-art semi-analytical multi-zone jet model BHJet with the `bljet` flavor. The goal of this work was to give us insight into the correlation between the evolution of the jet parameters and how they link to the accretion state of the source during outbursts. The results gave an evolving set of parameters that gave information on how the jet changed over time. Using these parameters, I theorized how the parameters that affected the photon index, mainly N_j, r_0, and T_e, could also affect the jet break frequency. I further discussed possible interpretations of the other parameters and potential reasons for why the evolution of the parameters from September 03 to September 12 differed from the given interpretation.

Further work on this topic would involve using the model on other sources and see if their parameters had similar correlations and/or evolved in a similar way. Of particular interest would be to apply the model to the sources that were studied in Koljonen et al. 2015 and claimed to hold a connection between the break frequency and photon index, and thus see if their parameters follow a similar evolution and/or correlation. Of particular interest would be the sources MAXI J1535-571 (T. D. Russell, M. Lucchini, et al. 2020) and MAXI J1820+070 (Rodi et al. 2021). Lastly, since various phenomenological parameters were used in the model, there was some difficulty giving physical interpretations for what these parameters described. Modeling the source again with future models that are able to give a more physical description of these jet properties could thus give a better, more physical understanding of the observed phenomena.

A Other Graphs

A.1 Individual SED fits

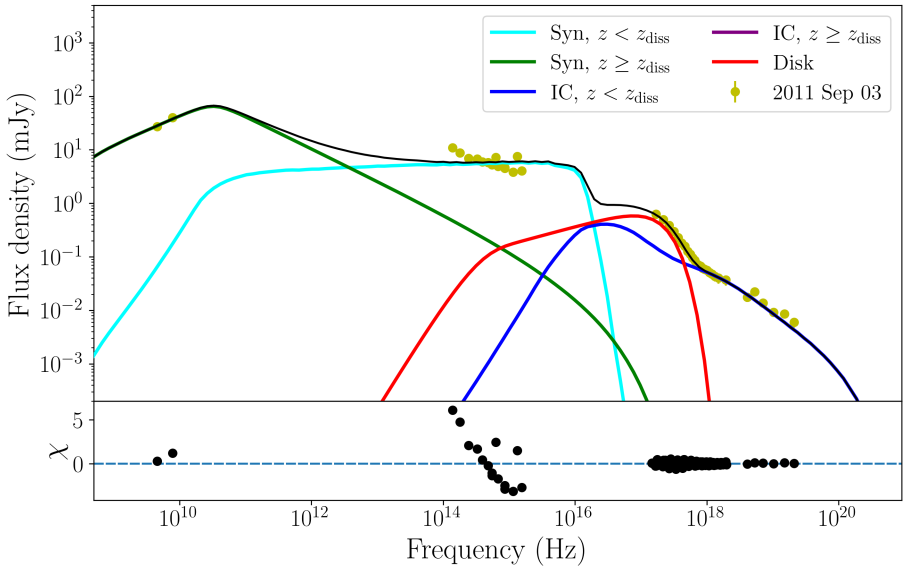

Figure 7: SED fit for September 03

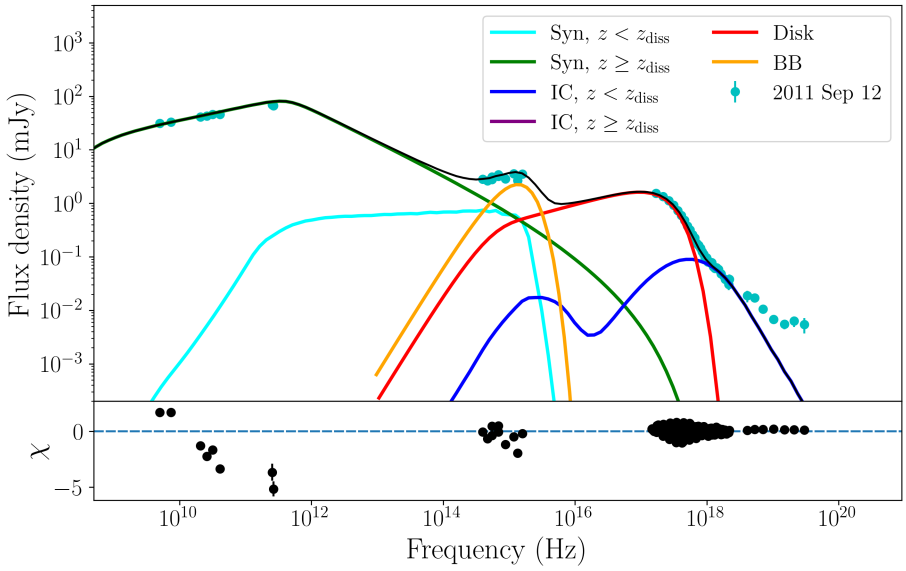

Figure 8: SED fit for September 12

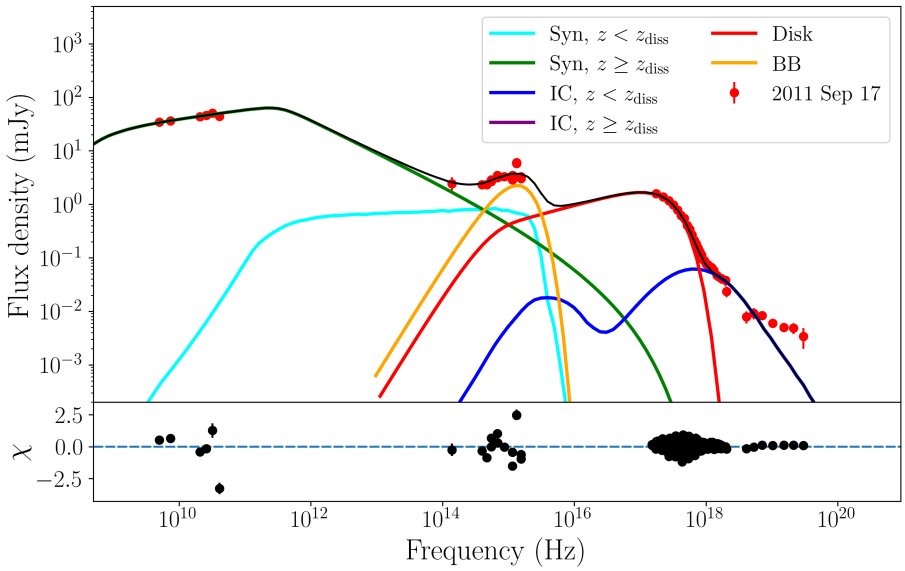

Figure 9: SED fit for September 17

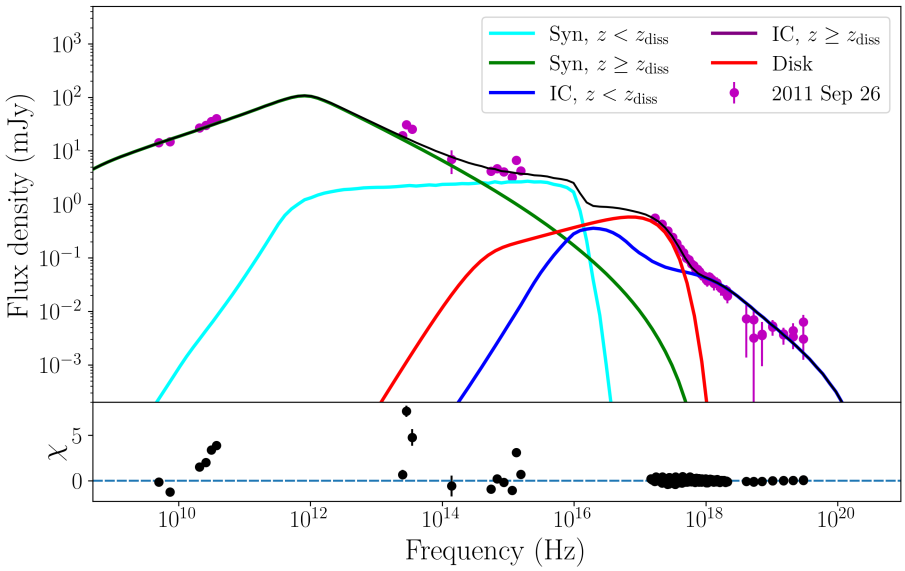

Figure 10: SED fit for September 26

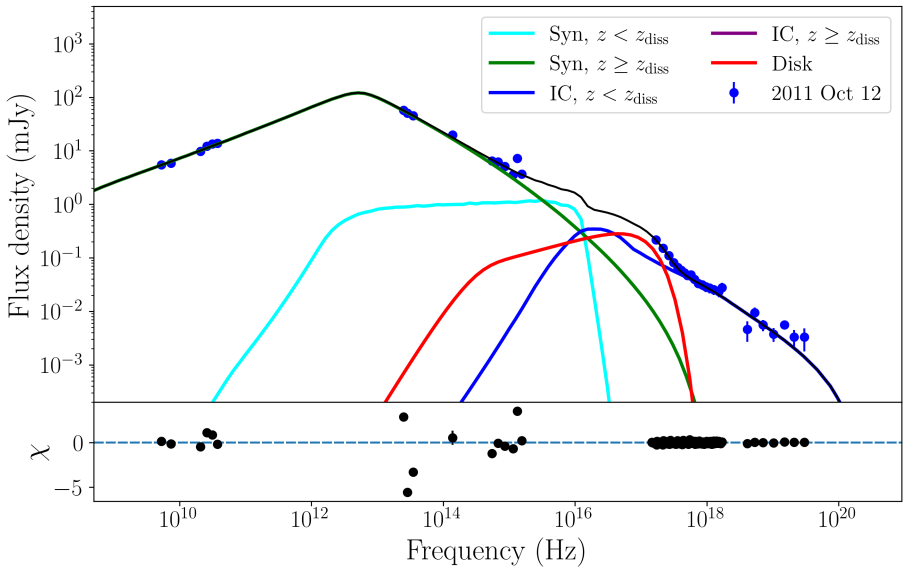

Figure 11: SED fit for October 12

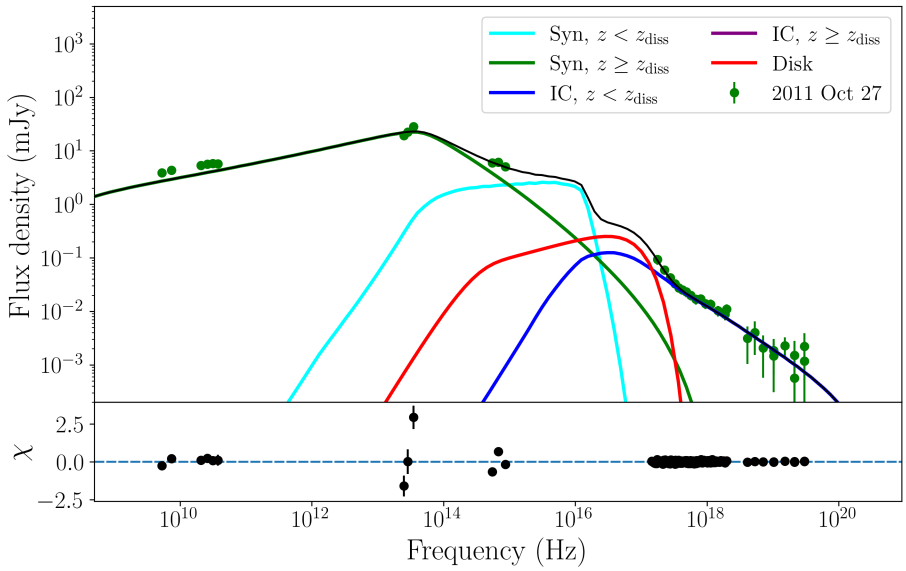

Figure 12: SED fit for October 27

A.2 Number density

Additional plots depicting the number density of the jet for each observing epoch. The left panel is plotted as a function of the dimensionless momentum ϱ, and the right panel is plotted as a function of the electron Lorentz factor. Each line shows the number density of a given zone along the jet, with the lighter hues being the zones further away from the nozzle.

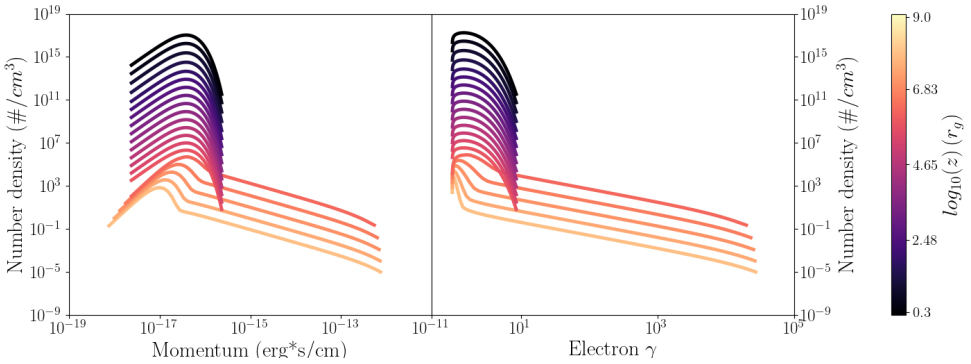

Figure 13: Particle distribution for September 03

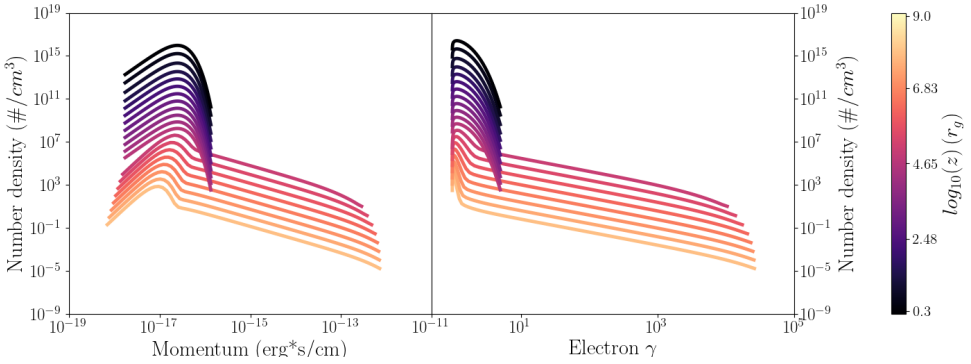

Figure 14: Particle distribution for September 12

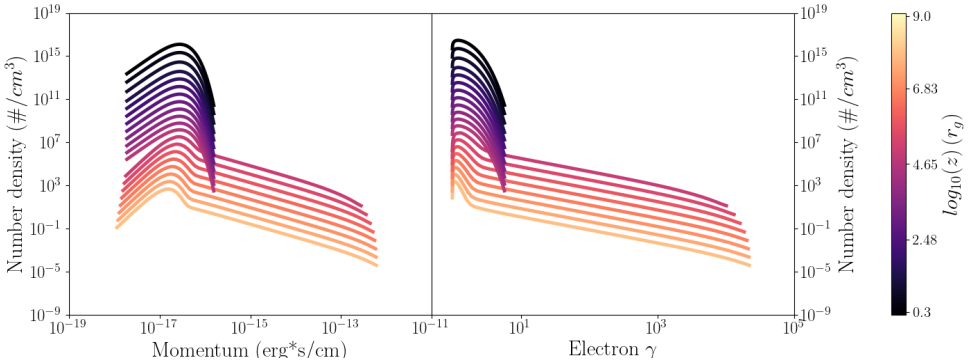

Figure 15: Particle distribution for September 17

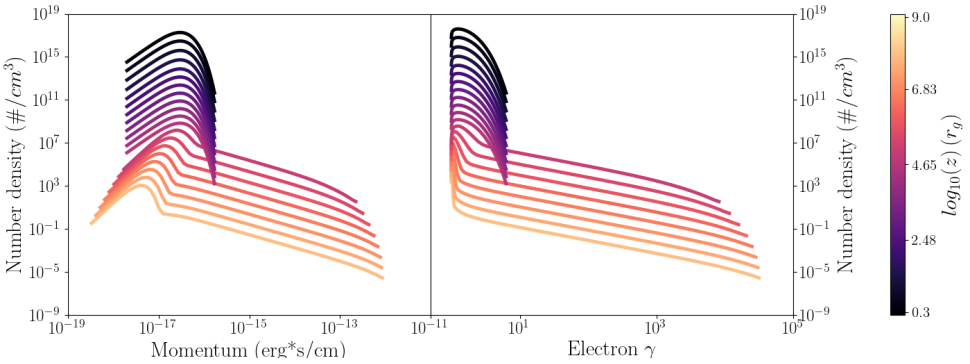

Figure 16: Particle distribution for September 26

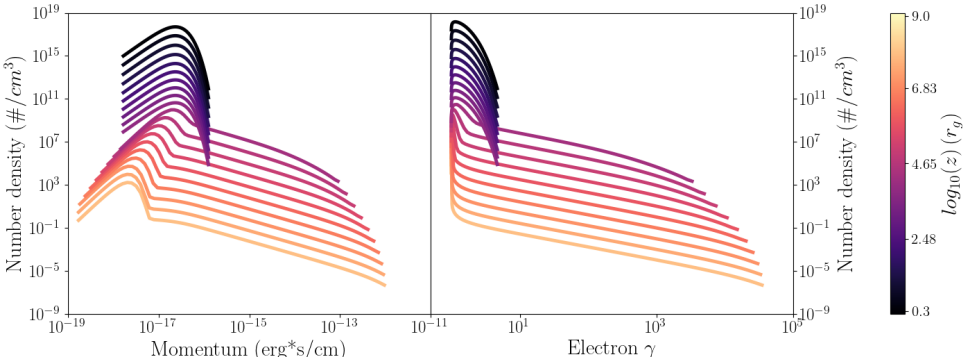

Figure 17: Particle distribution for October 12

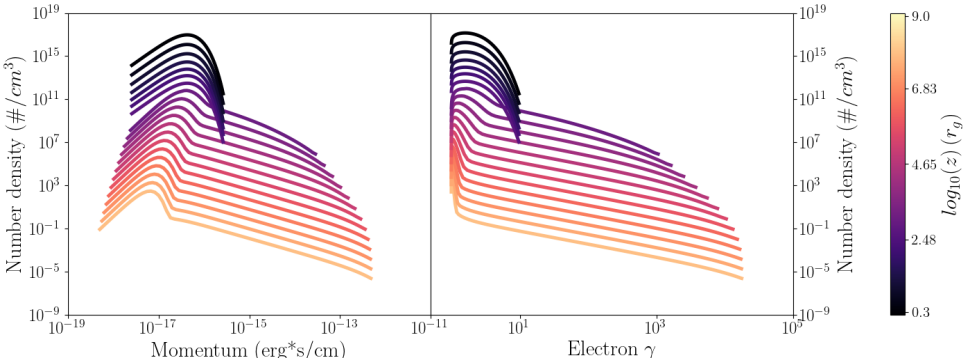

Figure 18: Particle distribution for October 27

B Evolution of parameters with s free

	03 Sep 2011	12 Sep 2011	17 Sep 2011	26 Sep 2011	12 Oct 2011	27 Oct 2011
Spectral state	Hard	HIMS	HIMS	HIMS	Hard	Hard
$N_j(10^{-2}L_{\rm Edd})$	$3.17^{+0.11}_{-0.10}$	4.40 ± 0.1	$2.14^{+0.08}_{-0.07}$	$5.15^{+0.01}_{-0.27}$	$5.99^{+0.80}_{-0.02}$	$3.10^{+0.26}_{-0.01}$
$r_0(R_g)$	$2.01^{0.01}_{-0.08}$	$27.37^{+1.27}_{-4.67}$	$10.05^{+9.77}_{-2.16}$	$5.66^{+0.19}_{-0.01}$	$2.55^{+0.31}_{-0.27}$	$2.21^{+0.14}_{-0.07}$
$z_{\rm diss}(R_g)$	$1.04^{+0.16}_{-0.01} \cdot 10^7$	$1.06^{+0.43}_{-0.21} \cdot 10^6$	$1.11^{+0.42}_{-0.58} \cdot 10^6$	$2.94^{+0.24}_{-0.05} \cdot 10^5$	$1.37^{+0.56}_{-0.61} \cdot 10^5$	$2.28^{+0.88}_{-0.09} \cdot 10^3$
T_e	$140.2^{+6.8}_{-2.9}$	$112.8^{+5.3}_{-2.3}$	$125.6^{+5.9}_{-11.9}$	$104.6^{+7.7}_{-13.0}$	$88.6^{+5.5}_{-0.5}$	$121.9^{+0.3}_{-8.1}$
f_{pl}	$41.5^{+1.0}_{-1.2}$	5.4 ± 0.1	$3.7^{+0.5}_{-1.1}$	$15.8^{+0.01}_{-0.3}$	$21.1^{+0.2}_{-0.7}$	$8.5^{+0.5}_{-0.2}$
s	1.75 ± 0.01	$2.60^{+0.05}_{-0.03}$	$2.29^{+0.03}_{-0.02}$	$2.19^{+0.03}_{-0.01}$	$2.19^{+0.01}_{-0.05}$	$2.45^{+0.03}_{-0.02}$
$L_{\rm disk}(10^{-2}L_{\rm Edd})$	$1.27^{+0.02}_{-0.01}$	4.16 ± 0.01	$4.69^{+0.01}_{-0.02}$	1.29 ± 0.02	$0.35^{+0.02}_{-0.01}$	$0.24^{+0.02}_{-0.06}$
$r_{\rm in}(R_g)$	$16.93^{+0.28}_{-0.62}$	$21.19^{+0.31}_{-0.25}$	$18.59^{+0.41}_{-0.34}$	$18.7^{+0.7}_{-0.8}$	$22.6^{+0.7}_{-1.3}$	$43.97^{+0.01}_{-6.25}$
χ^2/ d.o.f.	456.5/447	764.1/576	523.5/494	429.2/480	274.7/333	202.4/277
$\chi^2_{\rm red}$	1.02	1.33	1.06	0.89	0.83	0.73

Table 4: The free parameters and their values for each of the dates for s being set free.

	03 Sep 2011	12 Sep 2011	17 Sep 2011	26 Sep 2011	12 Oct 2011	27 Oct 2011
Spectral state	Hard	HIMS	HIMS	HIMS	Hard	Hard
$\alpha_{\rm thick}$	0.48	0.19	0.15	0.39	0.47	0.25
Γ	1.82	2.76	2.59	2.49	1.89	1.93
$\gamma_{\rm avg}$	1.48	1.38	1.16	1.34	1.30	1.40
τ	$0.80^{+0.05}_{-0.01}$	0.13	1.08	0.51 ± 0.04	$1.23^{+0.22}_{-0.25}$	0.62
$\log\nu_b$	10.82	11.81	11.71	12.21	12.71	13.80
$S_{\nu,b}$	127.9	73.18	66.51	121.3	121.4	25.6
$kT_{\rm disk}$(keV)	0.35	0.42	0.47	0.34	0.21	0.14

Table 5: Various properties of the jet and how they changed over time when s is set free

Nomenclature

Mbh	Black hole mass
θ	Inclination of the source
N_j	Power of the jet
r_0	Jet nozzle radius
$z_{\rm diss}$	Start of dissipation region
$z_{\rm acc}$	End of acceleration region
$z_{\rm max}$	Maximum length of jet region
$T_{\rm e}$	Lepton temperature in the jet base
$f_{\rm nth}$	Fraction of thermal particles accelerated into non-thermal tail
$f_{\rm pl}$	Parameter affecting the particle distribution and temperature after $z_{\rm diss}$
s	Slope of non-thermal tail
$f_{\rm heat}$	Shock heating parameter, increases $T_{\rm e}$ by a factor of $f_{\rm heat}$ at $z_{\rm diss}$
f_β	Sets the break Lorentz factor in the non-thermal tail
$f_{\rm sc}$	Sets $\gamma_{\rm max}$ in non-thermal tail if $\rm f_{\mathit{sc}} < 1$
$\beta_{\rm p}$	Ratio of lepton energy density to magnetic field density
$\sigma_{\rm acc}$	Leftover magnetization at $z_{\rm acc}$
$L_{\rm disk}$	Luminosity of the disk
$r_{\rm in}$	Inner radius of the accretion disk
γ_{acc}	Terminal Lorentz factor reached at z_{acc}
$\gamma_{\rm brk}$	The break Lorentz factor
$\alpha_{\rm thick}$	Optically thick spectral index
Γ	Photon index
γ_{avg}	Average Lorentz factor in the jet
τ	Optical thickness of the jet nozzle
$\nu_{\rm b}$	Break frequency
$S_{\nu,{\rm b}}$	Spectral flux at break frequency
$kT_{\rm disk}$	Temperature of the inner disk
ξ	Relativistic enthalpy

References

Blumenthal, G. R. and R. J. Gould (Apr. 1970). "Bremsstrahlung, Synchrotron Radiation, and Compton Scattering of High-Energy Electrons Traversing Dilute Gases". In: *Rev. Mod. Phys.* 42 (2), pp. 237–270. DOI: 10.1103/RevModPhys.42.237. URL: https://link.aps.org/doi/10.1103/RevModPhys.42.237.

Tananbaum, H. et al. (Oct. 1972). "Observation of a Correlated X-Ray Transition in Cygnus X-1". In: *The Astrophysical Journal* 177, p. L5. DOI: 10.1086/181042.

Shakura, N. I. and R. A. Sunyaev (Jan. 1973). "Black holes in binary systems. Observational appearance." In: *Astronomy & Astrophysics* 24, pp. 337–355.

Blandford, R. D. and A. Königl (Aug. 1979). "Relativistic jets as compact radio sources." In: *The Astrophysical Journal* 232, pp. 34–48. DOI: 10.1086/157262.

Konigl, A. (June 1980). "Relativistic gasdynamics in two dimensions". In: *Physics of Fluids* 23.6, pp. 1083–1090. DOI: 10.1063/1.863110.

Meyer, F. and E. Meyer-Hofmeister (1981). "On the elusive cause of cataclysmic variable outbursts". In: *Astronomy and Astrophysics* 104.

Cardelli, Jason A., Geoffrey C. Clayton, and John S. Mathis (Oct. 1989). "The Relationship between Infrared, Optical, and Ultraviolet Extinction". In: *The Astrophysical Journal* 345, p. 245. DOI: 10.1086/167900.

Falcke, H. and P. L. Biermann (Jan. 1995). "The jet-disk symbiosis. I. Radio to X-ray emission models for quasars." In: *Astronomy & Astrophysics* 293, pp. 665–682. DOI: 10.48550/arXiv.astro-ph/9411096. arXiv: astro-ph/9411096 [astro-ph].

Ghisellini, G., F. Haardt, and R. Svensson (June 1998). "Thermalization by synchrotron absorption in compact sources: electron and photon distributions". In: *Monthly Notices of the Royal Astronomical Society* 297.2, pp. 348–354. DOI: 10.1046/j.1365-8711.1998.01442.x. URL: https://doi.org/10.1046%2Fj.1365-8711.1998.01442.x.

Kubota, Aya et al. (Dec. 1998). "Evidence for a Black Hole in the X-Ray Transient GRS 1009-45". In: *Publications of the Astronomical Society of Japan* 50, pp. 667–673. DOI: 10.1093/pasj/50.6.667.

Tavecchio, Fabrizio, Laura Maraschi, and Gabriele Ghisellini (Dec. 1998). "Constraints on the Physical Parameters of TeV Blazars". In: *The Astrophysical Journal* 509.2, pp. 608–619. DOI: 10.1086/306526. arXiv: astro-ph/9809051 [astro-ph].

Dhawan, V., I. F. Mirabel, and L. F. Rodríguez (Nov. 2000). "AU-Scale Synchrotron Jets and Superluminal Ejecta in GRS 1915+105". In: *The Astrophysical Journal* 543.1, pp. 373–385. DOI: 10.1086/317088. arXiv: astro-ph/0006086 [astro-ph].

Houck, J. C. and L. A. Denicola (Jan. 2000). "ISIS: An Interactive Spectral Interpretation System for High Resolution X-Ray Spectroscopy". In: *Astronomical Data Analysis Software and Systems IX*. Ed. by Nadine Manset, Christian Veillet, and Dennis Crabtree. Vol. 216. Astronomical Society of the Pacific Conference Series, p. 591.

Lasota, Jean-Pierre (June 2001). "The disc instability model of dwarf novae and low-mass X-ray binary transients". In: *New Astronomy Reviews* 45.7, pp. 449–508. DOI: 10.1016/S1387-6473(01)00112-9. arXiv: astro-ph/0102072 [astro-ph].

Markoff, S., H. Falcke, and R. Fender (June 2001). "A jet model for the broadband spectrum of XTE J1118+480. Synchrotron emission from radio to X-rays in the Low/Hard spectral state".

In: *Astronomy & Astrophysics* 372, pp. L25–L28. DOI: 10.1051/0004-6361:20010420. arXiv: astro-ph/0010560 [astro-ph].

Stirling, A. M. et al. (Nov. 2001). "A relativistic jet from Cygnus X-1 in the low/hard X-ray state". In: *Monthly Notices of the Royal Astronomical Society* 327.4, pp. 1273–1278. DOI: 10.1046/j.1365-8711.2001.04821.x. arXiv: astro-ph/0107192 [astro-ph].

Vlahakis, Nektarios and Arieh Königl (Oct. 2003). "Relativistic Magnetohydrodynamics with Application to Gamma-Ray Burst Outflows. I. Theory and Semianalytic Trans-Alfvénic Solutions". In: *The Astrophysical Journal* 596.2, pp. 1080–1103. DOI: 10.1086/378226. arXiv: astro-ph/0303482 [astro-ph].

Fender, R. P., T. M. Belloni, and E. Gallo (Dec. 2004). "Towards a unified model for black hole X-ray binary jets". In: *Monthly Notices of the Royal Astronomical Society* 355.4, pp. 1105–1118. DOI: 10.1111/j.1365-2966.2004.08384.x. arXiv: astro-ph/0409360 [astro-ph].

Homan, Jeroen and Tomaso Belloni (Nov. 2005). "The Evolution of Black Hole States". In: *Astrophysics and Space Science* 300.1-3, pp. 107–117. DOI: 10.1007/s10509-005-1197-4. URL: https://doi.org/10.1007%2Fs10509-005-1197-4.

Jorstad, Svetlana G. et al. (Oct. 2005). "Polarimetric Observations of 15 Active Galactic Nuclei at High Frequencies: Jet Kinematics from Bimonthly Monitoring with the Very Long Baseline Array". In: *The Astronomical Journal* 130.4, pp. 1418–1465. DOI: 10.1086/444593. URL: https://doi.org/10.1086%2F444593.

Lourakis, Manolis (Jan. 2005). "A Brief Description of the Levenberg-Marquardt Algorithm Implemened by levmar". In: *A Brief Description of the Levenberg-Marquardt Algorithm Implemented by Levmar* 4.

Markoff, S., M. A. Nowak, and J. Wilms (Dec. 2005). "Going with the Flow: Can the Base of Jets Subsume the Role of Compact Accretion Disk Coronae?" In: *The Astrophysical Journal* 635.2, pp. 1203–1216. DOI: 10.1086/497628. arXiv: astro-ph/0509028 [astro-ph].

Lewin, Walter H. G. and Michiel van der Klis (2006). *Compact Stellar X-ray Sources*. Vol. 39.

Remillard, Ronald A. and Jeffrey E. McClintock (Sept. 2006). "X-Ray Properties of Black-Hole Binaries". In: *Annual Review of Astronomy and Astrophysics* 44.1, pp. 49–92. DOI: 10.1146/annurev.astro.44.051905.092532. URL: https://doi.org/10.1146%2Fannurev.astro.44.051905.092532.

Komissarov, Serguei S. et al. (Sept. 2007). "Magnetic acceleration of relativistic active galactic nucleus jets". In: *Monthly Notices of the Royal Astronomical Society* 380.1, pp. 51–70. DOI: 10.1111/j.1365-2966.2007.12050.x. arXiv: astro-ph/0703146 [astro-ph].

Matsuoka, Masaru et al. (Oct. 2009). "The MAXI Mission on the ISS: Science and Instruments for Monitoring All-Sky X-Ray Images". In: *Publications of the Astronomical Society of Japan* 61.5, pp. 999–1010. DOI: 10.1093/pasj/61.5.999. URL: https://doi.org/10.1093%2Fpasj%2F61.5.999.

Pushkarev, A. B. et al. (Oct. 2009). "Jet opening angles and gamma-ray brightness of AGN". In: *Astronomy &amp Astrophysics* 507.2, pp. L33–L36. DOI: 10.1051/0004-6361/200913422. URL: https://doi.org/10.1051%2F0004-6361%2F200913422.

Tchekhovskoy, Alexander, Jonathan C. McKinney, and Ramesh Narayan (June 2009). "EFFICIENCY OF MAGNETIC TO KINETIC ENERGY CONVERSION IN A MONOPOLE MAGNETOSPHERE". In: *The Astrophysical Journal* 699.2, pp. 1789–1808. DOI: 10.1088/0004-637x/699/2/1789. URL: https://doi.org/10.1088%2F0004-637x%2F699%2F2%2F1789.

Polko, P., D. L. Meier, and S. Markoff (Oct. 2010). "DETERMINING THE OPTIMAL LOCATIONS FOR SHOCK ACCELERATION IN MAGNETOHYDRODYNAMICAL JETS". In: *The Astrophysical Journal* 723.2, pp. 1343–1350. DOI: 10.1088/0004-637x/723/2/1343. URL: https://doi.org/10.1088%2F0004-637x%2F723%2F2%2F1343.

Miller-Jones, J. C. A. et al. (Sept. 2011). "EVLA radio detections of MAXI J1836-194 suggest it is a black hole X-ray binary". In: *The Astronomer's Telegram* 3628, p. 1.

Negoro, H. et al. (Aug. 2011). "MAXI/GSC and Swift/BAT detect a new hard X-ray transient MAXI J1836-194". In: *The Astronomer's Telegram* 3611, p. 1.

Russell, D. M., T. Belloni, et al. (Oct. 2011). "Bright mid-infrared detections of MAXI J1836-194 with VISIR on the VLT: brightening of the compact jet". In: *The Astronomer's Telegram* 3689, p. 1.

Sironi, Lorenzo and Anatoly Spitkovsky (Jan. 2011). "Particle Acceleration in Relativistic Magnetized Collisionless Electron-Ion Shocks". In: *The Astrophysical Journal* 726.2, 75, p. 75. DOI: 10.1088/0004-637X/726/2/75. arXiv: 1009.0024 [astro-ph.HE].

Strohmayer, T. E. and E. A. Smith (Aug. 2011). "RXTE Observations of MAXI J1836-194". In: *The Astronomer's Telegram* 3618, p. 1.

Coriat, M., R. P. Fender, and G. Dubus (2012). "Revisiting a fundamental test of the disc instability model for X-ray binaries". In: *Monthly Notices of the Royal Astronomical Society* 424.3, pp. 1991–2001. DOI: 10.1111/j.1365-2966.2012.21339.x.

Polko, P., D. L. Meier, and S. Markoff (Oct. 2012). "Linking accretion flow and particle acceleration in jets – I. New relativistic magnetohydrodynamical jet solutions including gravity". In: *Monthly Notices of the Royal Astronomical Society* 428.1, pp. 587–598. DOI: 10.1093/mnras/sts052. URL: https://doi.org/10.1093%2Fmnras%2Fsts052.

Reis, R. C. et al. (May 2012). "Suzaku Observation of the Black Hole Candidate Maxi J1836-194 in a Hard/Intermediate Spectral State". In: *The Astrophysical Journal* 751.1, 34, p. 34. DOI: 10.1088/0004-637X/751/1/34. arXiv: 1111.6665 [astro-ph.HE].

Böttcher, M. et al. (May 2013). "Leptonic and Hadronic Modeling of Fermi-detected Blazars". In: *The Astrophysical Journal* 768.1, 54, p. 54. DOI: 10.1088/0004-637X/768/1/54. arXiv: 1304.0605 [astro-ph.HE].

Russell, D. M., T. D. Russell, et al. (May 2013). "An Evolving Compact Jet in the Black Hole X-Ray Binary MAXI J1836-194". In: *The Astrophysical Journal Letters* 768.2, L35, p. L35. DOI: 10.1088/2041-8205/768/2/L35. arXiv: 1304.3510 [astro-ph.HE].

Sironi, Lorenzo, Anatoly Spitkovsky, and Jonathan Arons (June 2013). "THE MAXIMUM ENERGY OF ACCELERATED PARTICLES IN RELATIVISTIC COLLISIONLESS SHOCKS". In: *The Astrophysical Journal* 771.1, p. 54. DOI: 10.1088/0004-637x/771/1/54. URL: https://doi.org/10.1088%2F0004-637x%2F771%2F1%2F54.

Polko, Peter, David L. Meier, and Sera Markoff (Jan. 2014). "Linking accretion flow and particle acceleration in jets – II. Self-similar jet models with full relativistic MHD gravitational mass". In: *Monthly Notices of the Royal Astronomical Society* 438.2, pp. 959–970. DOI: 10.1093/mnras/stt2155. URL: https://doi.org/10.1093%2Fmnras%2Fstt2155.

Russell, T. D., R. Soria, J. C. A. Miller-Jones, et al. (Jan. 2014). "The accretion–ejection coupling in the black hole candidate X-ray binary MAXI J1836-194". In: *Monthly Notices of the Royal Astronomical Society* 439.2, pp. 1390–1402. DOI: 10.1093/mnras/stt2498. URL: https://doi.org/10.1093%2Fmnras%2Fstt2498.

Russell, T. D., R. Soria, C. Motch, et al. (Feb. 2014). "The face-on disc of MAXI J1836-19472". In: *Monthly Notices of the Royal Astronomical Society* 439.2, pp. 1381–1389. DOI: 10.1093/mnras/stt2480. URL: https://doi.org/10.1093%2Fmnras%2Fstt2480.

Sironi, Lorenzo and Anatoly Spitkovsky (Feb. 2014). "RELATIVISTIC RECONNECTION: AN EFFICIENT SOURCE OF NON-THERMAL PARTICLES". In: *The Astrophysical Journal* 783.1, p. L21. DOI: 10.1088/2041-8205/783/1/l21. URL: https://doi.org/10.1088%2F2041-8205%2F783%2F1%2Fl21.

Boccardi, B. et al. (Dec. 2015). "The stratified two-sided jet of Cygnus A". In: *Astronomy &amp Astrophysics* 585, A33. DOI: 10.1051/0004-6361/201526985. URL: https://doi.org/10.1051%2F0004-6361%2F201526985.

Koljonen, K. I. I. et al. (Dec. 2015). "A Connection between Plasma Conditions near Black Hole Event Horizons and Outflow Properties". In: *The Astrophysical Journal* 814.2, 139, p. 139. DOI: 10.1088/0004-637X/814/2/139. arXiv: 1510.08122 [astro-ph.HE].

Sironi, Lorenzo, Maria Petropoulou, and Dimitrios Giannios (Apr. 2015). "Relativistic jets shine through shocks or magnetic reconnection?" In: *Monthly Notices of the Royal Astronomical Society* 450.1, pp. 183–191. DOI: 10.1093/mnras/stv641. URL: https://doi.org/10.1093%2Fmnras%2Fstv641.

Connors, R. M. T. et al. (Dec. 2016). "Mass-scaling as a method to constrain outflows and particle acceleration from low-luminosity accreting black holes". In: *Monthly Notices of the Royal Astronomical Society*, stw3150. DOI: 10.1093/mnras/stw3150. URL: https://doi.org/10.1093%2Fmnras%2Fstw3150.

Mertens, F. et al. (Oct. 2016). "Kinematics of the jet in M 87 on scales of 100–1000 Schwarzschild radii". In: *Astronomy &amp Astrophysics* 595, A54. DOI: 10.1051/0004-6361/201628829. URL: https://doi.org/10.1051%2F0004-6361%2F201628829.

Crumley, Patrick et al. (May 2017). "The jet-disk symbiosis withoutimaximal jets/i: 1D hydrodynamical jets revisited". In: *Astronomy &amp Astrophysics* 601, A87. DOI: 10.1051/0004-6361/201630229. URL: https://doi.org/10.1051%2F0004-6361%2F201630229.

Crumley, P et al. (Jan. 2019). "Kinetic simulations of mildly relativistic shocks – I. Particle acceleration in high Mach number shocks". In: *Monthly Notices of the Royal Astronomical Society* 485.4, pp. 5105–5119. DOI: 10.1093/mnras/stz232. URL: https://doi.org/10.1093%2Fmnras%2Fstz232.

Lucchini, M, T D Russell, et al. (Dec. 2020). "Correlating spectral and timing properties in the evolving jet of the microblazar MAXI J1836-194". In: *Monthly Notices of the Royal Astronomical Society* 501.4, pp. 5910–5926. DOI: 10.1093/mnras/staa3957. URL: https://doi.org/10.1093%2Fmnras%2Fstaa3957.

Russell, T. D., M. Lucchini, et al. (Nov. 2020). "Rapid compact jet quenching in the Galactic black hole candidate X-ray binary MAXI J1535-571". In: *Monthly Notices of the Royal Astronomical Society* 498.4, pp. 5772–5785. DOI: 10.1093/mnras/staa2650. arXiv: 2008.11216 [astro-ph.HE].

Rodi, J. et al. (Mar. 2021). "A Broadband View on Microquasar MAXI J1820+070 during the 2018 Outburst". In: *The Astrophysical Journal* 910.1, 21, p. 21. DOI: 10.3847/1538-4357/abdfd0. arXiv: 2101.10767 [astro-ph.HE].

Lucchini, M, C Ceccobello, et al. (Oct. 2022). "Bhjet: a public multizone, steady state jet thermal corona spectral model". In: *Monthly Notices of the Royal Astronomical Society* 517.4, pp. 5853–5881. DOI: 10.1093/mnras/stac2904. URL: https://doi.org/10.1093%2Fmnras%2Fstac2904.